

JGR Solid Earth

RESEARCH ARTICLE

10.1029/2023JB027550

Key Points:

- We investigate geomagnetic field behavior at high paleolatitude ($\sim 80^\circ\text{N}$) at the end of the Cretaceous Normal Superchron (CNS)
- We present a paleodirectional data set from 78 lava flows (resp. 57 directional groups), emplaced 84–89 Ma in north-eastern Eurasia
- We show that the dispersion of virtual geomagnetic poles at high latitude is $\sim 15\%$ lower during the CNS than for the past 10 Myr

Correspondence to:

F. Lhuillier,
florian.lhuillier@lmu.de

Citation:

Lhuillier, F., Lebedev, I. E., Tikhomirov, P. L., & Pavlov, V. E. (2024). High-latitude geomagnetic secular variation at the end of the Cretaceous Normal Superchron recorded by volcanic flows from the Okhotsk-Chukotka Volcanic Belt. *Journal of Geophysical Research: Solid Earth*, 129, e2023JB027550. <https://doi.org/10.1029/2023JB027550>

Received 26 JUL 2023

Accepted 5 DEC 2023

Author Contributions:

Conceptualization: F. Lhuillier, V. E. Pavlov

Data curation: I. E. Lebedev, P. L. Tikhomirov, V. E. Pavlov

Funding acquisition: F. Lhuillier, V. E. Pavlov

Investigation: I. E. Lebedev, P. L. Tikhomirov, V. E. Pavlov

Methodology: I. E. Lebedev, P. L. Tikhomirov

Validation: F. Lhuillier, V. E. Pavlov


Writing – original draft: F. Lhuillier, V. E. Pavlov

Writing – review & editing: F. Lhuillier, I. E. Lebedev, P. L. Tikhomirov, V. E. Pavlov

© 2023 The Authors.

This is an open access article under the terms of the [Creative Commons Attribution-NonCommercial License](https://creativecommons.org/licenses/by/4.0/), which permits use, distribution and reproduction in any medium, provided the original work is properly cited and is not used for commercial purposes.

High-Latitude Geomagnetic Secular Variation at the End of the Cretaceous Normal Superchron Recorded by Volcanic Flows From the Okhotsk-Chukotka Volcanic Belt

F. Lhuillier¹ , I. E. Lebedev², P. L. Tikhomirov², and V. E. Pavlov^{2,3}

¹Department of Earth and Environmental Sciences, Ludwig-Maximilians-Universität, Munich, Germany, ²Schmidt Institute of Physics of the Earth, Russian Academy of Sciences, Moscow, Russia, ³Kazan (Volga) Federal University, Kazan, Russia

Abstract The Cretaceous Normal Superchron (CNS, 84–121 Ma) is a singular period of the geodynamo's history, identified by a prolonged absence of polarity reversals. To better characterize the paleosecular variation (PSV) of the geomagnetic field at the end of this interval, we sampled seven continuous sequences of lava flows from the Okhotsk-Chukotka Volcanic Belt, emplaced 84–89 Ma in the vicinity of the Kupol ore deposit (NE Russia). From a collection of 1,024 paleomagnetic cores out of 82 investigated lava flows, we successfully determined the paleodirections of 78 lava flows, which led to 57 directional groups after removing the serial correlations. The resulting paleomagnetic pole is located at 170.0°E , 76.8°N ($A_{95} = 5.2^\circ$, $N = 57$), in good agreement with previous estimates for north-eastern Eurasia. Aiming at quantifying PSV at a reconstructed paleolatitude (λ) of $\sim 80^\circ\text{N}$, we obtained a virtual geomagnetic pole (VGP) scatter $S_b = 21.5^\circ|_{19.3^\circ}^{24.0^\circ}$ ($N = 57$), the value of which was corrected for within-site dispersion and is little dependent on the choice of the selection criteria. Compared to previous paleodirectional data sets characterizing PSV at various paleolatitudes during the CNS, our S_b estimate confirms a relative latitudinal increase $S_b(\lambda = 90^\circ)/S_b(\lambda = 0^\circ)$ on the order of 2–2.5. Focusing on PSV at high paleolatitude within the 70° – 90° range, we show that S_b was $\sim 15\%$ lower at the end of the CNS than during the past 10 Myr, confirming that the singular polarity regime of the geodynamo observed during the CNS is likely accompanied with reduced PSV.

Plain Language Summary Compared to the last 10 million years during which Earth's magnetic field stochastically reversed its polarity ~ 4 times per million year, the Cretaceous Normal Superchron (CNS, 84–121 Ma) represents an anomalously long period of stable polarity, the understanding of which is crucial to constrain the working of the geodynamo. In this effort to better characterize the paleosecular variation (PSV) of the geodynamo, we investigated the paleomagnetic record of lava flow sequences from the Okhotsk-Chukotka Volcanic Belt (NE Russia) emplaced 84–89 Ma at high paleolatitude. First, we obtained that the dispersion of virtual paleomagnetic poles (VGP), used as a proxy for PSV, is 2–2.5 times as high at the paleopole as at the paleoequator. Second, we showed that VGP scatter at high paleolatitude was $\sim 15\%$ lower at the end of the CNS than during the last 10 million years, confirming a potential link between polarity regime and PSV.

1. Introduction

The geomagnetic field, produced by thermo-chemical convection of an electrically conducting fluid in Earth's outer core, experienced significant changes in its rate of polarity reversals throughout geologic times. In particular, two end-member polarity regimes have been identified during the Phanerozoic (e.g., Gallet & Pavlov, 2016). On the one hand, three superchrons—the Cretaceous Normal Superchron (CNS, 84–121 Ma), the Permo-Carboniferous Reverse Superchron (267–318 Ma) and the Ordovician Reverse Superchron (463–485 Ma)—are defined as prolonged periods with stable polarity (e.g., Ogg, 2020; Pavlov & Gallet, 2005). On the other, two hyperactivity events, with more than 10 reversals per million year, were hypothesized during the Middle Jurassic (155–171 Ma; e.g., Tivey et al., 2006; Tominaga et al., 2008) and the Cambrian (e.g., Duan et al., 2018; Gallet et al., 2019). Besides these extremal events, the reversal frequency f_{rev} generally lies between one to four per million year (e.g., Lowrie & Kent, 2004; Ogg, 2020). Generally, the geomagnetic field can also experience fluctuations in its average intensity F and its spatiotemporal variability during stable periods (termed hereafter paleosecular variation, PSV). Whether changes in f_{rev} , F and PSV occur in a coupled or decoupled way is a vivid matter of debate among paleomagnetists (e.g., Cox, 1968; Dubrovine et al., 2019; Eid et al., 2022; Kulakov et al., 2019; Lhuillier, Lebedev, et al., 2023; Lhuillier, Shcherbakov, & Sycheva, 2023; McFadden et al., 1991; Tarduno

et al., 2002). Conceptually, numerical dynamo simulations tend to support an increase in F with decreasing f_{rev} or the amplitude of PSV, with a coupling controlled in first approximation by the vigor of convection (e.g., Driscoll & Olson, 2009; Lhuillier & Gilder, 2013). Practically, identifying such correlations in the paleomagnetic record is nevertheless difficult for at least two reasons. First, the geodynamo is likely more complex than the predictions from numerical dynamo simulations. Second, the requirements to get robust statistics of the geodynamo's state may not always be fulfilled due to sparse and/or uncertain paleomagnetic records.

For a collection of N rapidly-cooled and time-independent volcanic units, PSV is traditionally quantified by the angular standard deviation

$$S = \sqrt{\frac{1}{N-1} \sum_{i=1}^N \Delta_i^2} \quad (1)$$

of the virtual geomagnetic poles (VGPs), where Δ_i is the angular distance of the mean VGP of the i th volcanic unit from the mean paleomagnetic pole of the study (Cox, 1970). Due to the variable precision of the directional distributions between the paleomagnetic sites, Equation 1 is often corrected for within-site dispersion to yield a more robust estimate of the between-site dispersion

$$S_b = \sqrt{\frac{1}{N-1} \sum_{i=1}^N \left(\Delta_i^2 - \frac{S_{wi}^2}{n_i} \right)} \quad (2)$$

where S_{wi} is the angular standard deviation of the individual VGPs within the i th volcanic unit (McFadden et al., 1991). Retrospectively, the choice of studying the dispersion of VGPs rather than of directions can be justified by the fact that the distributions of VGPs are predicted to be more fisherian than those of directions, based on the outcomes of numerical dynamo simulations and statistic field models (e.g., Lhuillier & Gilder, 2013; Tauxe & Kent, 2004). This prediction is confirmed for at least the past 30 Myr, during which the distributions of paleodirections are strongly elongated in the meridian plane at low paleolatitude (Lhuillier & Gilder, 2019).

Generally, it has long been recognized that S_b varies with site paleolatitude, with the dual consequence that (a) S_b can only be compared at the same paleolatitude, or (b) a paleolatitudinal profile of S_b is needed to produce a global characterization of PSV at a given epoch (e.g., Cromwell et al., 2018; de Oliveira et al., 2021). The dependency of S_b with site paleolatitude λ is commonly described by model G of McFadden et al. (1988)

$$S_b(\lambda) = \sqrt{a^2 + (b\lambda)^2}, \quad (3)$$

where a and b are the two parameters to be fitted. The original interpretation of McFadden et al. (1988)—variations in a (resp. b) caused by equatorially symmetric (resp. equatorially antisymmetric) terms of the spherical harmonic expansion of the field—has been criticized for several decades (e.g., Hulot & Gallet, 1996) but model G is still used as a comparative framework between studies.

Getting a clear description of the geodynamo's state during the CNS is a challenging task due to diverse contradictions in the observations. In terms of reconstructed dipole strength, values up to three times higher during the CNS than the average value during the Cenozoic were reported from Thellier-style experiments on single plagioclase crystals (e.g., Tarduno et al., 2001, 2002) or on submarine volcanic glasses (Tauxe & Staudigel, 2004), whereas values indistinguishable from the average value during the Cenozoic were also repeatedly reported from Thellier-style experiments on non-glassy whole-rock samples (e.g., Dodd et al., 2015; Prévot et al., 1990; Shcherbakova et al., 2012) or submarine volcanic glasses (e.g., Di Chiara et al., 2021; Granot et al., 2007; Pick & Tauxe, 1993). Single-crystal API determinations thus supports the existence of a correlation between chron duration and dipole moment over the past 160 Myr (Tarduno & Cottrell, 2005). In contrast, most of the recent statistical analyses of the whole-rock API determinations tend to refute the existence of such a correlation over this time interval (e.g., Bobrovnikova et al., 2022; Di Chiara et al., 2021; Eid et al., 2022; Ingham et al., 2014; Lhuillier, Lebedev, et al., 2023; Lhuillier, Shcherbakov, & Sycheva, 2023), with the exception of Kulakov et al. (2019).

In a seminal study, McFadden et al. (1991) compiled and analyzed a wide collection of S_b values derived from igneous rocks, to describe the potential changes in PSV over the past 190 My. In particular, they proposed a lower equatorial value of S_b (i.e., a lower value of the a parameter in Equation 3) together with greater latitudinal increase of S_b (i.e., a larger value of the b parameter in Equation 3) during the CNS than during periods with

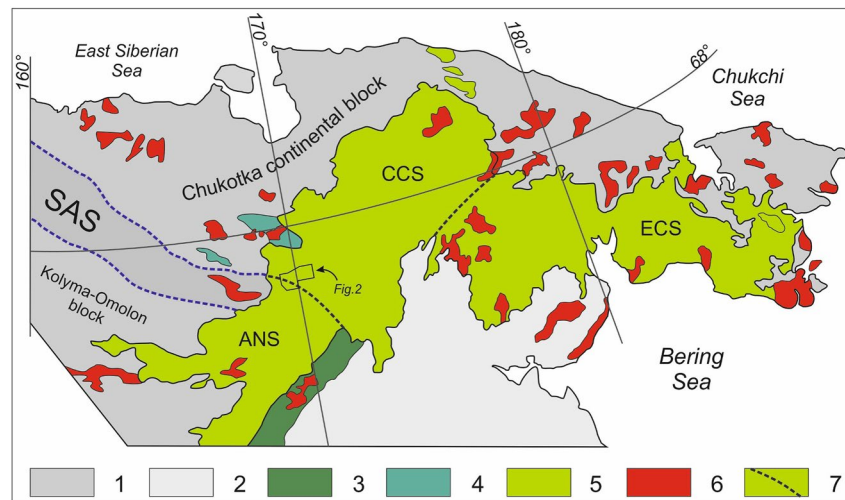


Figure 1. Tectonic schema of Chukotka. (1) Verkhoyansk–Chukotka fold region. (2) Koryak–Kamchatka fold region. (3) Uda-Murgal volcanic arc. (4) Tytylveem post-collisional clastic sediments and volcanic sequences. (5) Okhotsk-Chukotka volcanic belt (OCVB). (6) Large Cretaceous granitic intrusions. (7) Boundaries of the OCVB segments defined by Belyi (1977): Anadyr segment, Central Chukotka segment and East Chukotka segment. SAS stands for South Anyui Suture.

more frequent reversals. Tarduno et al. (2002), followed by Biggin et al. (2008) and Doubrovine et al. (2019), confirmed the latitudinal increase of S_p during the CNS. However, Doubrovine et al. (2019) stressed that parameter b may be an unreliable proxy for reversal frequency, based on the observation that S_p is latitudinally invariant during the pre-CNS period but has a latitudinal profile over the past 10 Myr akin to the one during CNS. Generally, it must be recognized that 10 out of the 20 available estimates of S_p during the CNS were computed on less than 25 cooling units, which may not be enough to guarantee the convergence of the results (e.g., Lhuillier & Gilder, 2013); only four studies fulfill the desirable convergence criteria with more than 50 cooling units.

In an effort to improve the characterization of the geodynamo's state during the CNS, we present in this paper new palaeodirectional results obtained from sequences of lava flows from the Okhotsk-Chukotka Volcanic Belt (OCVB), emplaced at high paleolatitude at the end of the CNS. Fulfilling modern paleomagnetic standards in terms of sampling methods and number of available samples per cooling unit, this contribution updates the preliminary results of Lebedev et al. (2021, 2022), and accompanies the paleointensity study conducted by Bobrovnikova et al. (2022).

2. Geological Setting

The OCVB is a prominent subduction-related magmatic province in the north-east of Eurasia. It covers an area of ca. 450,000 km² from the western coast of the Sea of Okhotsk to the eastern margin of the Chukotka Peninsula, and was active during a prolonged time interval ranging from ~110 to ~70 Ma (e.g., Akinin & Miller, 2011; Tikhomirov et al., 2012). As shown in Figure 1, the studied area is located near the boundary between the Anadyr segment and the Central Chukotka segment of the OCVB defined by Belyi (1977).

The basement of the OCVB crops out ~20 km north-west from the studied area and includes complexes of two major tectonic zones. On the one hand, the South Anyui Suture (SAS) zone is dominated by densely folded Triassic to Early Cretaceous clastic and volcanic strata. This suture is thought to be the remnant of an oceanic basin that formerly separated the Chukotka microcontinent from the Kolyma-Omolon block accreted to the Siberian platform near the end of the Jurassic (e.g., Amato et al., 2015; Sokolov et al., 2015). The age of the latest significant compression event in the SAS zone is constrained by the youngest detrital zircons extracted from syn-collisional sandstones, yielding U-Pb ages of ca. 125 Ma (Amato et al., 2015). On the other hand, the sedimentary complexes thought to be formed at the passive margin of the Chukotka microcontinent (Nokleberg et al., 2000; Tuchkova et al., 2020) are located to the north of the SAS zone and consist of moderately folded Triassic clastic strata. The SAS zone and Chukotka passive margin are separated by a major fault zone interpreted as a SW vergent thrust (Amato et al., 2015) but retaining records of significant superposed dextral strike-slip deformations (Sokolov

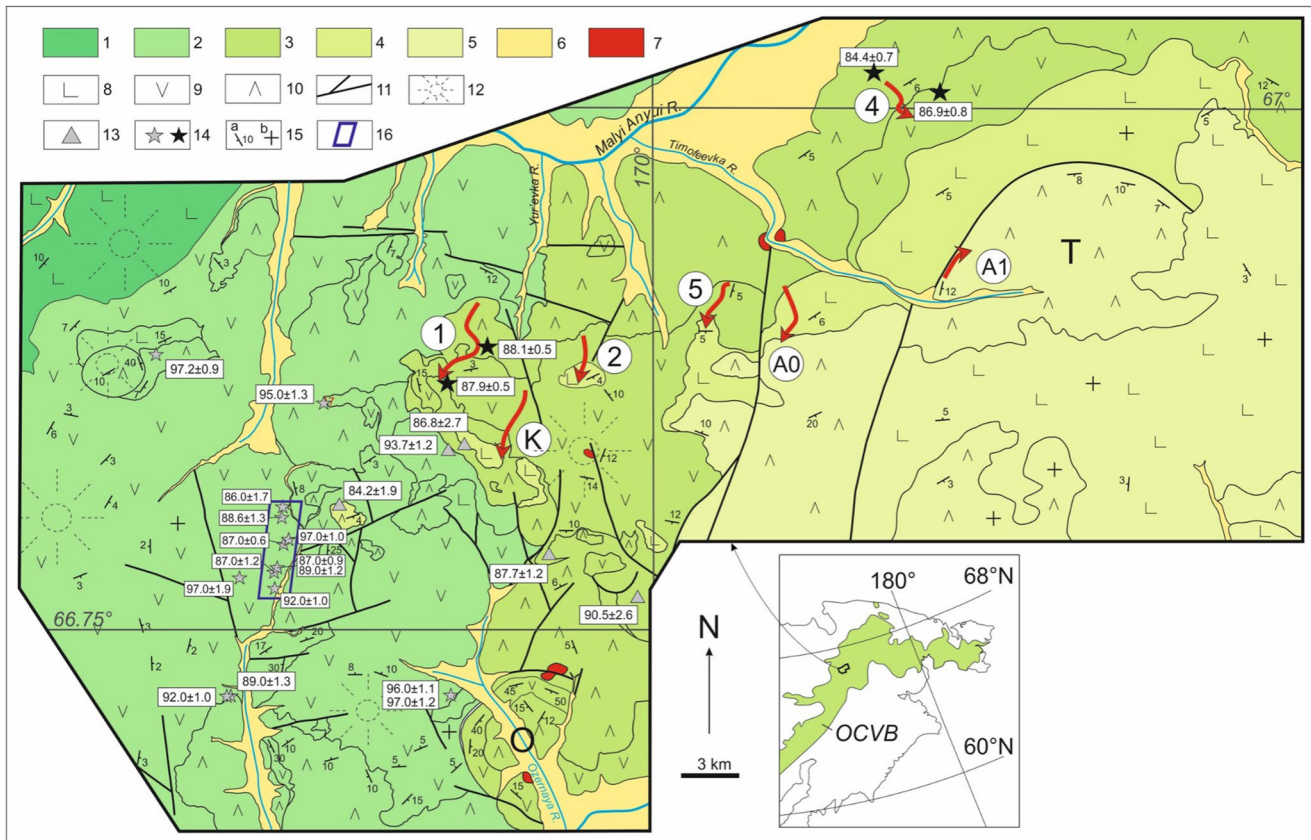


Figure 2. Geological map of the investigated area. (1–7) Stratigraphic units of the Okhotsk-Chukotka Volcanic Belt defined by Tikhomirov (2020a, 2020b): (1) Vilkovskaya suite, presumably Albian; (2) Mechkereva suite, Cenomanian; (3) Kayemravaam suite, Turonian-Santonian; (4) Kovalenko suite, Santonian; (5) uppermost volcanic units; (6) Quaternary strata; and (7) intrusive and subvolcanic bodies. (8–10) Major varieties of volcanic rocks: (8) basalts; (9) andesites; (10) rhyolites. (11) Major faults. (12) Relics of stratovolcano edifices. (13–14) radioisotopic age determinations from previous studies (see Tikhomirov et al., 2021 for a review): (13) $^{40}\text{Ar}/^{39}\text{Ar}$ determinations, (14) U-Pb determinations, where the black stars depict the dates constraining the sections investigated in this study. (15) Strike and dip of the volcanic strata: (a) inclined strata; (b) horizontal strata. (16) Approximate boundaries of the Kupol ore field. The red arrows describe the seven investigated sections. The letters O and T denote the Ozernaya and Timofeevka calderas.

et al., 2015). The both complexes are unconformably overlain by syn- and post-collisional Late Jurassic to Early Cretaceous marine and continental clastic sediments (up to 3 km thick; e.g., Sokolov, 2010), as well as by Early Cretaceous Volcanic sequences (up to 1 km thick, 115–121 Ma; e.g., Thomson et al., 2021). These volcanics are considered as the remnants of the deeply eroded NW-directed Tytylveem post-collisional magmatic belt (Tikhomirov et al., 2017).

The volcanic sequences of the OCVB (74–106 Ma; e.g., Akinin & Miller, 2011; Tikhomirov et al., 2020) unconformably overlie all pre-Albian complexes. Within the studied area shown in Figure 2, the sequences averagely dip 5° – 10° southeast, toward the inner zone of the volcanic belt. In the absence of vestiges of compressional tectonics, the monocline likely results from the subsidence related with the discharge of magmatic chambers (Tikhomirov et al., 2020). The local departures of the bedding attitude from the general SE trend are ascribed to dissected paleotopography and/or local manifestations of caldera tectonics (e.g., Cole et al., 2005). The latter effect is most pronounced for the Ozernaya caldera that shows a dip angle up to 50° at the margins of this structure, reducing to 10° – 15° inside and outside the edifice. The larger Timofeevka caldera (ca. 12 km in diameter) is bounded by an arcuate fault at its north but do not show any signs of significant displacements.

The stratigraphic model of the studied area, improved by the $^{40}\text{Ar}/^{39}\text{Ar}$ and U-Pb age determinations from Tikhomirov et al. (2021), comprises four major suites which are from the bottom to the top: (a) the Vilkovskaya suite of andesites and basaltic andesites (presumably 100–105 Ma); (b) the Mechkereva suite of andesites with 10%–15% of silicic volcanics (92–98 Ma); (c) the Kayemravaam suite of andesites with 30%–40% of silicic rocks (84–90 Ma); and (d) the Kovalenko suite of olivine basalts (only constrained by a single $^{40}\text{Ar}/^{39}\text{Ar}$ date of

86.8 ± 2.7 Ma). In the eastern part of the studied area, the basaltic lavas from the Kovalenko suite are overlain by a thick (>300 m) sequence of ignimbrites and basaltic lavas that have not been radioisotopically dated but may be coeval with the youngest OCVB volcanics (81–84 Ma; Sakhno et al., 2010; Tikhomirov et al., 2012). The total thickness of the OCVB volcanics within the study area exceeds 700 m, as evidenced by the deep drilling at the Kupol ore deposit (Tikhomirov, 2020a, 2020b).

3. Method

3.1. Paleomagnetic Sampling

Following preliminary paleomagnetic field work in the Chukotka region (Lebedev et al., 2021, 2022), we identified seven sections that deserved further investigation. Sections 1, 2, and K are located in the upper reaches of the Yurievka river, a left tributary of the Malyi Anyui river (Figure 2). The volcanic flows consist of basaltic lavas and gently dip (up to 5°) toward SE. Sections A0, A1, 4, and 5 are located in the upper reaches of the Timofeevka river, a left tributary to the Malyu Anyui river (Figure 2). The volcanic flows also consist of basaltic lavas (although with occasional occurrences of acidic varieties) and dip 4°–12° toward SE. Each section represents a continuous series of 4–22 lava flows. Six of the seven sections are natural exposures of the Kayemravaam and Kovalenko suites, whereas Section A1 likely represent the very base of the uppermost volcanics units (Figure 2). The age of the sections is constrained by four U-Pb determinations conducted on zircons from rhyolitic lavas or ignimbrites (black stars in Figure 2; Tikhomirov et al., 2021). Two determinations yielded 88.1 ± 0.5 (2σ) Ma and 87.9 ± 0.5 (2σ) Ma for the base and roof of Section 01, 86.9 ± 0.8 (2σ) Ma and 84.4 ± 0.7 (2σ) Ma for the base and middle of Section 04 (Tikhomirov et al., 2021). Combined with stratigraphic analysis, it indicates that all the volcanic piles investigated in this study were likely emplaced between ~89 and ~84 Ma.

During a paleomagnetic campaign conducted in summer 2021, we resampled the flows documented in Lebedev et al. (2022), as well as three additional flows for Section 1, six additional flows for Section 2, and nine additional flows for Section 5 (Figure 3). We failed to resample one of the five flows from Section 4. In comparison to the previous collection of samples obtained by Lebedev et al. (2022), which mostly consisted of hand-picked blocks oriented with a magnetic compass, all the samples from this study are 1-inch paleomagnetic cores obtained with a gas-powered drill and oriented using a Pomeroy fixture. We drilled in total 1,024 cores from 82 flows, with 10–15 cores per flow. By sampling different parts of the flows, we wanted to average out within-flow variability and a posteriori check that the studied outcrops were not affected by local tectonic processes. Note that this effort to obtain 10–15 cores per flow did not come at the expense of fewer flows sampled. When permitted by weather conditions (~70% of the cases), the azimuth of the cores was determined using a sun compass. Otherwise, the azimuth of the cores was reconstructed using a laser mounted on a theodolite. As shown in Figure 3h, three angles are needed to obtain the true azimuth of the cores: (a) α is the angle between a remote reference point and the gnomon of the orienting head, measured with the theodolite; (b) β is the angle between the z -axis of the core and the shadow of the gnomon produced by the laser, measured with the protractor of the orienting head; (c) γ is the angle between the geographic north and the remote reference point, determined from the GPS coordinates of the theodolite and of the reference point. The uncertainty of the method is mostly controlled by the uncertainty on γ . In this study, using a GPS device with a horizontal accuracy of 3 m and a remote point with a distance of at least 500 m, we can ensure that the final uncertainty on the azimuth of the core does not exceed 1°. Empirically, a comparison of 100 pairs of azimuth readings made using both a sun compass and a laser theodolite showed good agreement between the two methods (mean angular difference of 0.3° with a standard deviation of 2.3°).

Due to the regional specificities of the erosional processes, the volcanic rocks sampled in this study were much better exposed on gentle hillsides than along the banks of the rivers. We made sure that the sampled blocks were not tilted by frost heaving and/or solifluction. This was facilitated by the excellent quality of the outcrops in the tundra, offering the possibility to trace the exposed flow contacts for several tens of meters and to directly measure the bedding attitude. In several cases where a single flow was associated with a visible topographic scarp, we calculated the bedding attitude from three points using the detailed topographic map together with satellite images. Generally, we claim that the measured dip corresponds to post-emplacment dip due to large-scale tectonics rather than initial dip due to the emplacement of the flows on a tilted surface. This is corroborated by the fact that similar dips were observed on the scale of several kilometers; initial dips would conversely follow the terrane's irregularities.

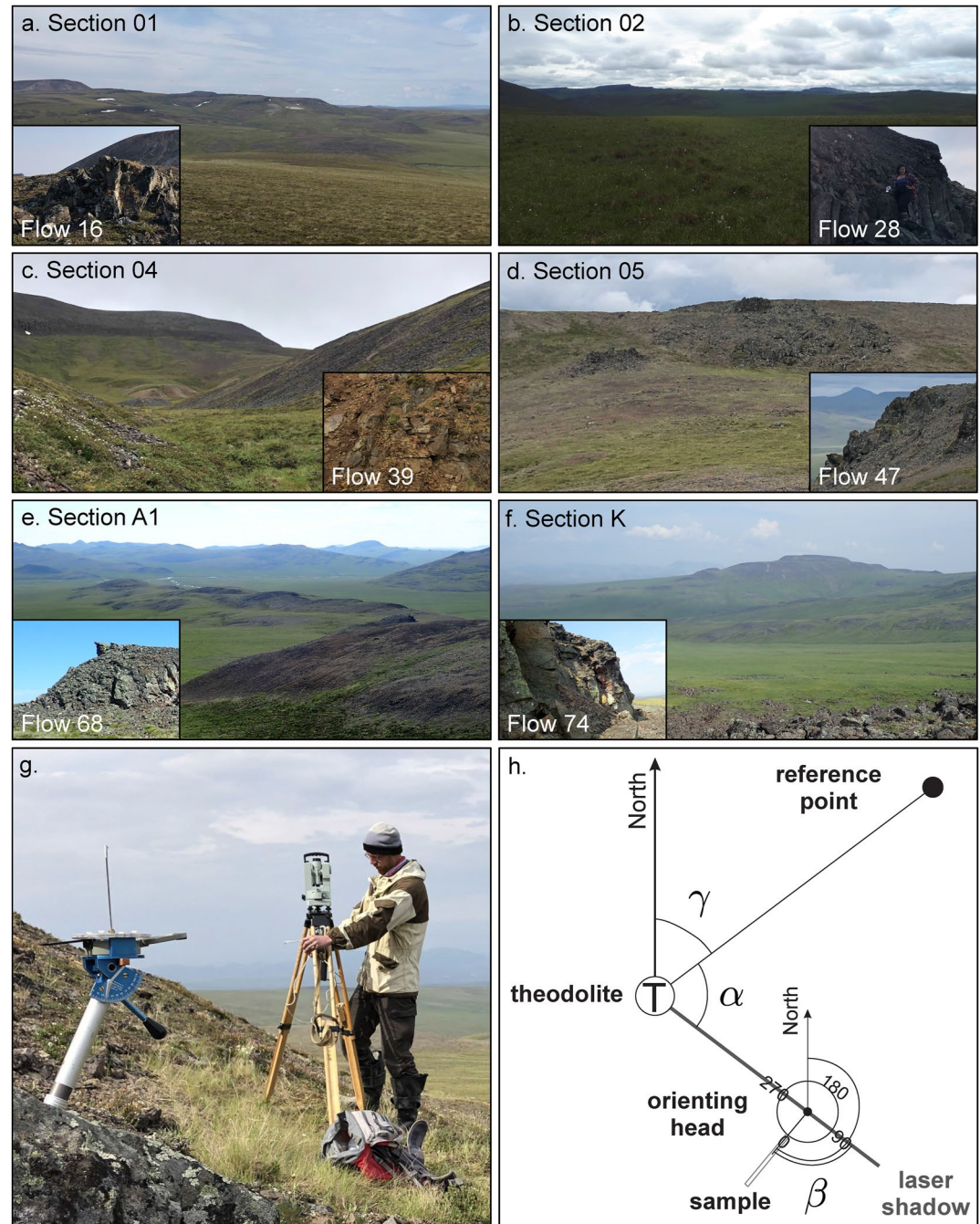


Figure 3. Overview of the investigated sections. (a–f) Field photographs of the investigated sections with representative examples of sampled outcrops in the insets. (g–h) Field photograph and sketch of the method used to determine the true azimuth of the cores using a laser theodolite, in the absence of sun exposure.

3.2. Rock-Magnetic Experiments and Microscopic Observations

Hysteresis and back-field curves were measured at the “Laboratory of Main Geomagnetic Field and Petromagnetism” of the Schmidt Institute of Physics of the Earth of the Russian Academy of Sciences (IPE-RAS, Moscow, Russia) or at the Ludwig-Maximilians-Universität (LMU, Munich, Germany) using a LakeShore Vibrating Sample Magnetometer (VSM). From these experiments, the ratios of the remanent saturation magnetization (M_{RS}) to the saturation magnetization (M_S) and of the remanent coercive force (H_{CR}) to the coercive force (H_C) were computed to assess the hypothetical domain structure of the magnetic grains in the Day diagram (Day

et al., 1977). To characterize the thermomagnetic behavior of the magnetic grains, continuous $M_s(T)$ curves were recorded during heating/cooling in air from room temperature to 600°C, at IPE-RAS in a laboratory field of 450 mT using a VSM designed by Y. K. Vinogradov, or at LMU in a laboratory field of 300 mT using a Variable Field Translation Balance designed by N. Petersen. The Curie points T_C of the ferrimagnetic phases were associated with the minima of the first-derivative of the heating branches of the $M_s(T)$ curves (e.g., Fabian et al., 2013). Finally, to further characterize the nature and oxidation degree of the magnetic grains, scanning electron microscopy (SEM) was performed at IPE-RAS on 10 representative samples using a TESCAN MIRA device equipped with an energy dispersive X-ray spectrometer.

3.3. Paleomagnetic Measurements

All remanence values were measured at IPE-RAS in a magnetically shielded room using a 2G Enterprise cryogenic magnetometer (Veselovskiy et al., 2022). All samples were demagnetized by alternating field (AF) treatment in 15 steps up to 125 mT using a 2G Enterprise degausser. Additionally, a sister specimen from one sample per lava flow was thermally (TH) demagnetized in 12–15 steps up to 600°C using a Magnetic Measurements TD80 furnace. The demagnetization data were visualized using vector endpoint diagrams (Zijderveld, 1967) and the characteristic remanent magnetization (ChRM) was fitted by principal component analysis (Kirschvink, 1980) using the PMGSC software (Enkin, 2003). The mean and dispersion of the individual directions were computed using Fisher's statistics (Fisher, 1953). To identify the volcanic flows that erupted during a short outburst of activity and may represent a quasi-instantaneous geomagnetic snapshot, we determined directional groups (DGs) using the algorithm proposed by Chenet et al. (2008). To ascertain the pristine nature of the ChRM, we performed the direction correction (DC) fold test (Enkin, 2003) as well as the bootstrap fold test (Tauxe & Watson, 1994).

4. Results

4.1. Magnetic Mineralogy

The bulk hysteresis properties, summarized in a Day diagram (Figure 4a), reveal that the majority of the samples lie in the region usually associated with pseudo-single domain behavior. The points tend to closely follow the single-domain (SD)/multidomain (MD) mixing curves of magnetite proposed by Dunlop (2002), with the exception of four points measured for Flows 02 and 03 from Section 01. In terms of thermomagnetic behavior (Figures 4b–4g), samples can schematically be separated into four groups. Lava flows from group #1 (~50% of the case, black solid lines in Figure 4b–4g) are characterized by the presence of a single Curie point above 500°C and nearly reversible behavior (Figures 5b, 5c, 5f, 5g, 5j, 5k, and 5n). They correspond to the lower parts of Sections 02, 05, and A1; the upper parts of Sections 01 and A0; the central parts of Sections 04 and K. Lava flows from group #2 (~20% of the cases, red dash-dotted lines in Figures 4b–4g) are characterized by the presence of a dominant Curie point lower than 300°C and nearly reversible behavior (Figures 5e and 5h). They correspond to the upper part of Section 05 and the top flow of Section 02. The remaining lava flows are heterogeneously characterized by the presence of two ferrimagnetic phases. On the one hand, the lava flows from group #3 (~20% of the cases, blue dotted lines in Figures 4b–4g) have a lower Curie point around 375–425°C and show gentle decrease in M_s upon cooling (Figures 5a, 5i, 5l, and 5m), suggestive of the coexistence of two titanomagnetite phases. They correspond to the lower parts of Sections 01, A0, and K, as well as the upper part of Section A1. On the other hand, the lava flows from group #4 (~10% of the cases, dashed green lines in Figures 4b–4g) have a lower Curie point around 230°C and show an irreversible increase in M_s upon cooling (Figures 5d and 5o), suggestive of the inversion of titanomaghemite to low-titanium titanomagnetite (e.g., Özdemir, 1987). They correspond to the upper part of Section 02 and the top flow of Section K.

Based on SEM observations conducted on 10 representative samples, we associate oxy-exsolved titanomagnetite (Figures 6a–6c) with the high-temperature phase ($T_C > 500^\circ\text{C}$) from groups #1 and #3. Despite having a Curie point close to the one of magnetite, Flow 47 from Section 05 (Figure 6d) is singular in the sense that it does not display euhedral oxy-exsolved titanomagnetite grains like in Figures 6a–6c. This apparent contradiction can be removed by the presence of titanomagnetite inclusions (of several μm size) within host pyroxene grains (Figures 7a and 7b). Detailed SEM and microprobe observations indicate that the titanomagnetite inclusions present nanoscale inhomogeneities that are interpreted as fine ilmenite lamellae (Figures 7c–7e). We thus speculate that the remanent magnetization of this flow is mainly carried by titanomagnetite grains, exsolved from host

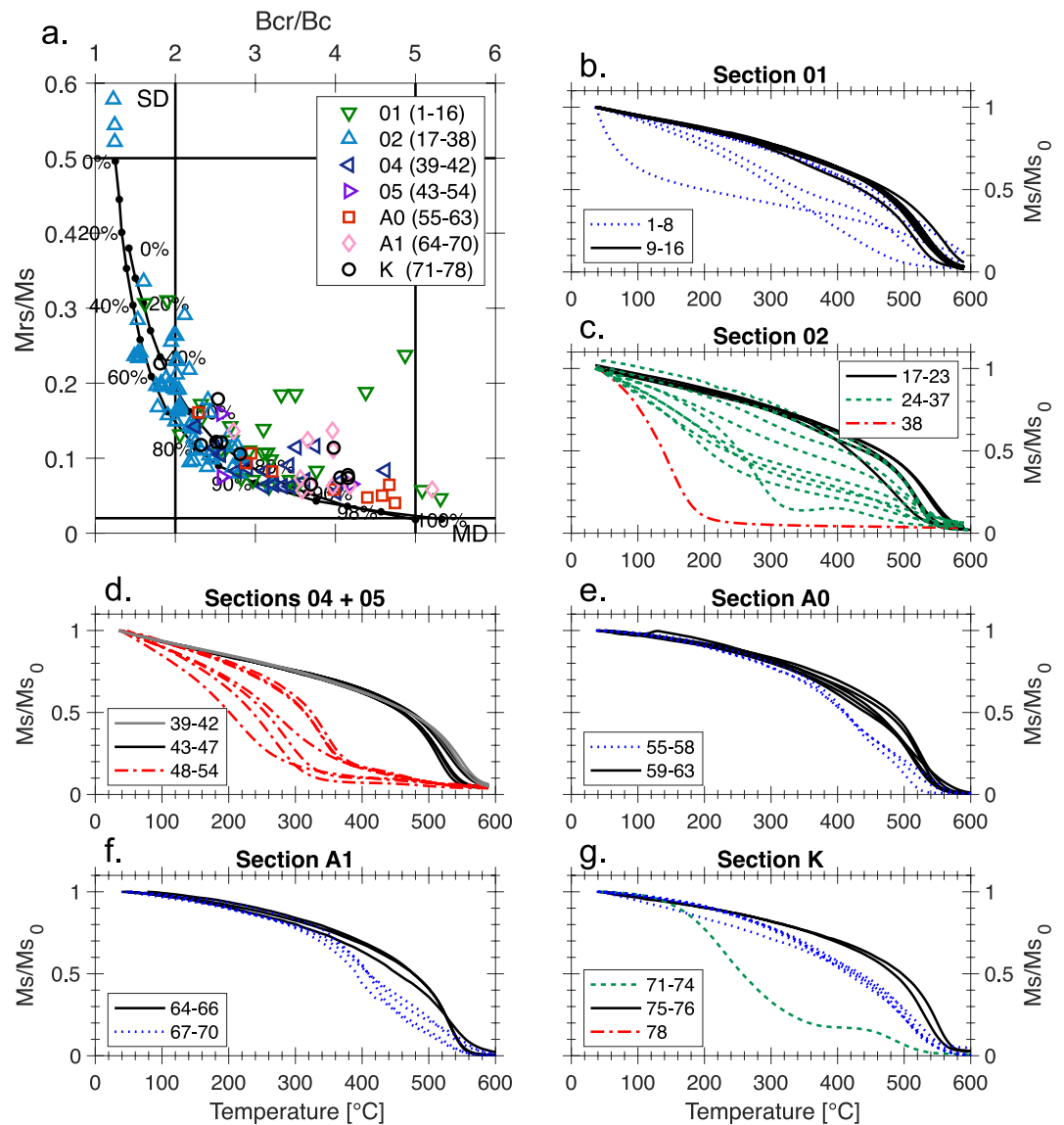


Figure 4. Rock-magnetic properties of the investigated lava flows. (a) Day diagram with single-domain (SD)/multidomain (MD) mixing curves for magnetite proposed by Dunlop (2002). (b–g) Heating branches of $M_s(T)$ curves for representative lava flows of the seven investigated sections. As explained in Section 4.1, lava flows were classified into four groups: #1 (black solid lines; $T_C > 500^{\circ}\text{C}$); #2 (red dash-dotted lines; $T_C < 300^{\circ}\text{C}$); #3 (blue dotted lines; $T_{C1} \approx 400^{\circ}\text{C}$ and $T_{C2} > 500^{\circ}\text{C}$); #4 (green dashed lines; $T_{C1} \approx 230^{\circ}\text{C}$ and $T_{C2} > 400^{\circ}\text{C}$).

pyroxene grains during the cooling of lava. These titanomagnetite inclusions likely experienced high-temperature oxidation (e.g., Gao et al., 2019), as revealed by the presence of fine ilmenite lamellae and titanium-poor areas. On the contrary, the remanence carriers associated with the low-temperature phase ($T_C < 300^{\circ}\text{C}$) from groups #2 and #4 were likely exposed to low-temperature oxidation, as revealed by the presence of shrinkage cracks (Figure 6f; e.g., Petersen & Vali, 1987). Finally, the remanence carriers from group #3, characterized by the coexistence of two stable high-temperature phases, may partly be explained by dual-phase titanomagnetite grains (Figure 6c).

4.2. Paleomagnetic Results

For one control sample per lava flow, AF and TH demagnetizations yielded consistent paleodirections in terms of angular distance δ between each pair of specimens (Figure 8). For 78 investigated samples, we obtained a median

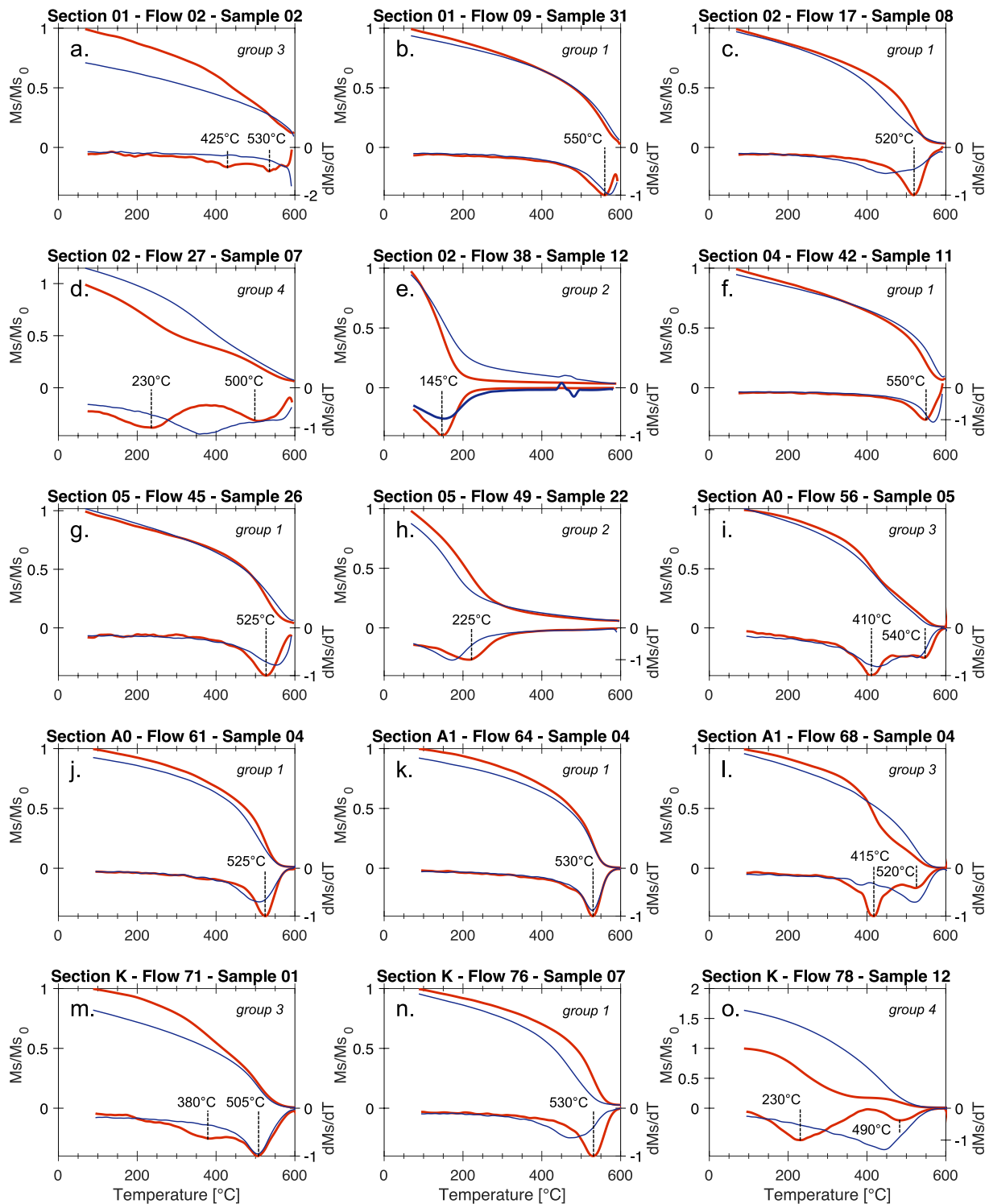


Figure 5. Thermomagnetic behavior of the saturation magnetization. Representative examples are shown for each of the four groups (15 sets) identified in Figure 4. For each panel, the upper axis shows the heating (thick red line) and cooling (thin blue line) branches of the normalized $M_s(T)$ curve, whereas the lower axis shows the normalized derivative dM_s/dT using the same color-coding. The interpreted Curie points correspond to minima of dM_s/dT .

value of 3.9° ($N = 78$), with an interquartile range (IQR) of 3.0° . Using the maximum angular deviation (MAD) as a proxy for the linearity of the PCA fits, we observed that AF demagnetizations (median MAD of 1.1° ; IQR of 1.0°) were slightly more efficient than TH demagnetization (median MAD of 2.3° , IQR of 2.0°) to remove

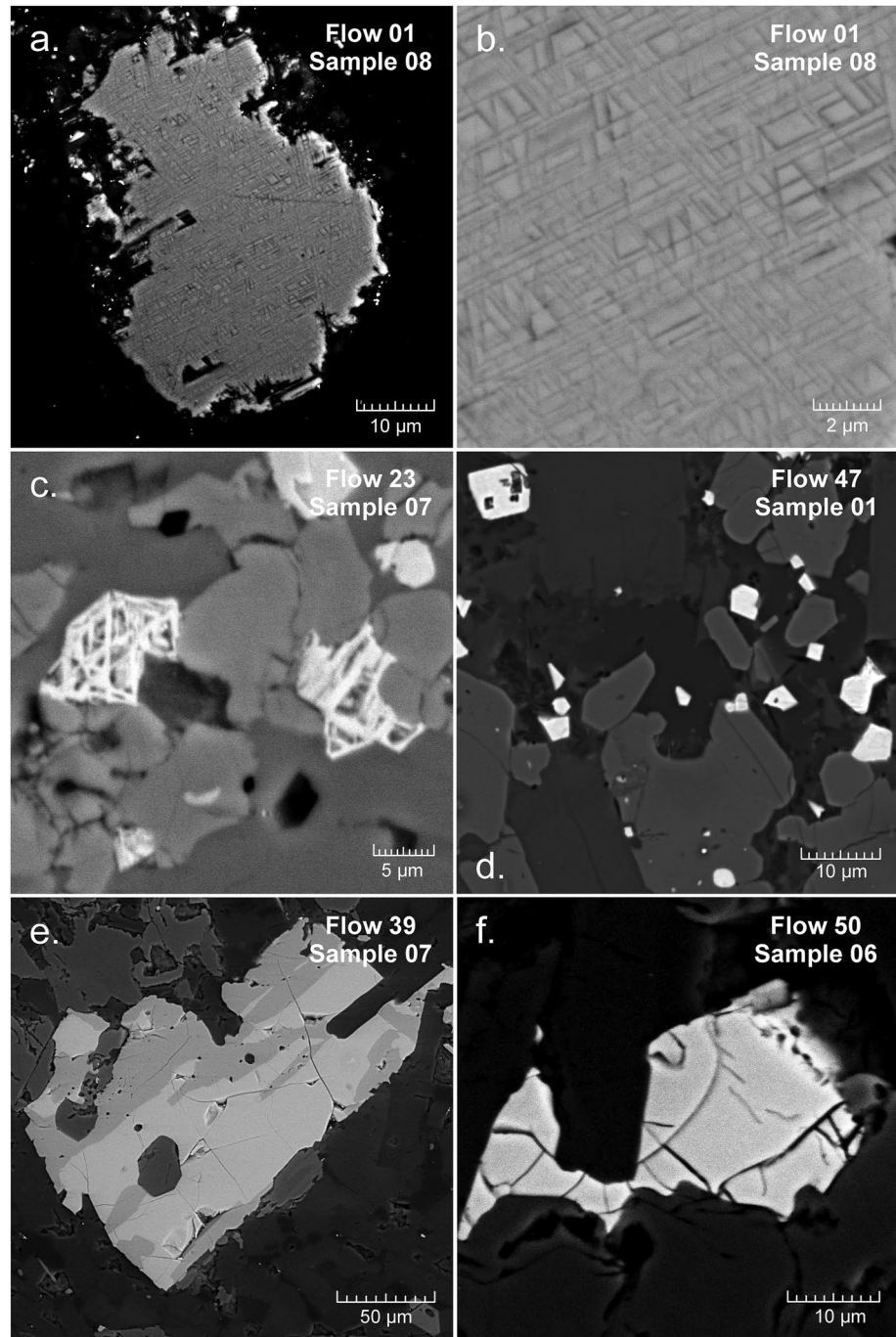


Figure 6. Scanning electron microscopy of titanomagnetite grains. (a–c) Exsolution lamellae of ilmenite within titanomagnetite grains, characteristic of high-temperature oxidation. (d) Seemingly unoxidized titanomagnetite grains. (e) Possible coexistence of two ferrimagnetic phases within multidomain titanomagnetite grain. (f) Shrinkage cracks within titanomagnetite grain.

secondary components. The angular distance $\theta = 0.9^\circ$ between the mean directions of the AF and TH demagnetization sets does not exceed the critical value $\theta_c = 5.7^\circ$ at which the null hypothesis of a common mean would be rejected with 95% confidence (Watson, 1983), indicating that viscous overprints—optimally removed by TH demagnetization—were equally well removed by AF demagnetization. Generally, the temperature spectra of the TH demagnetization experiments (Figure 9, red squares) were in good agreement with the $M_s(T)$ curves from neighboring samples within the same flow (Figure 5). With the exception of Flow 9 with a nearly linear decrease

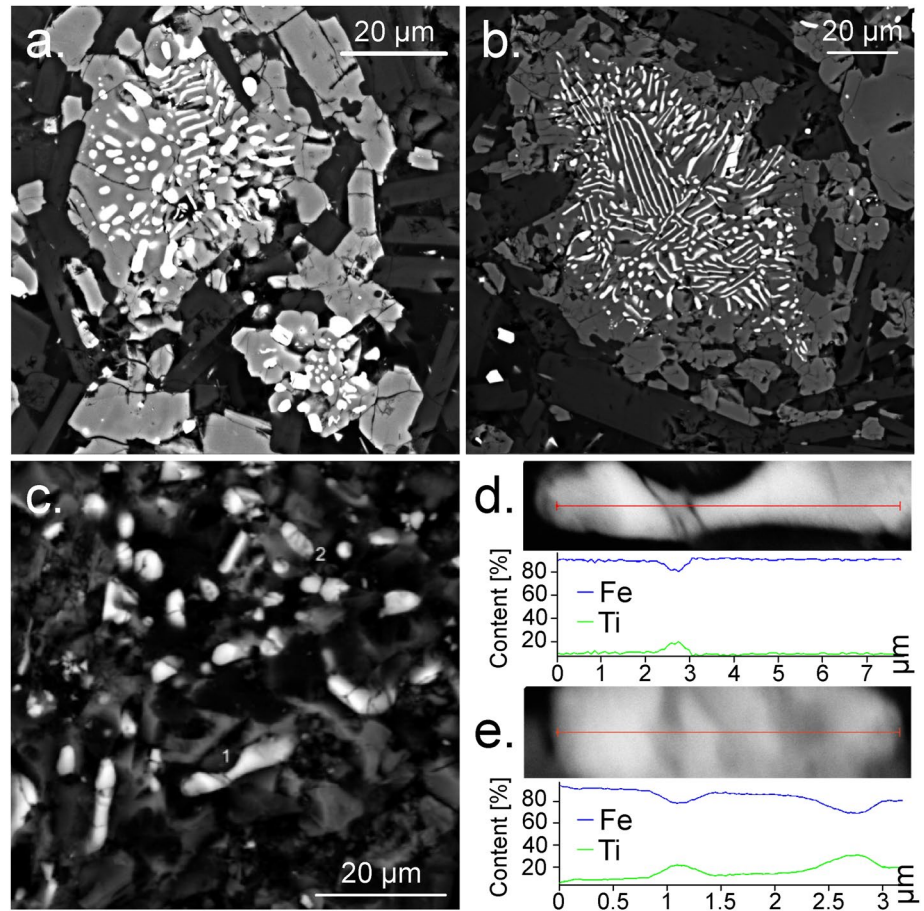


Figure 7. Scanning electron microscopy and microprobe analysis of pyroxene grains with oxy-exsolved titanomagnetite inclusions. (a, b) Microphotographs of two characteristic pyroxene grains. (c–e) Microprobe analysis of two titanomagnetite inclusions. Inclusions 1 and 2 showed in panel c are investigated in panels d and e. All the observations are from Flow 47 (Sample 01).

in M_{RS} (Figure 9b), samples from group 1 had a sharp decrease in M_{RS} between 550 and 600°C (Figures 9c, 9f, 9g, 9k, 9l, and 9o). Samples from group 2 unblocked most of their remanent magnetization below 300°C (Figures 9e and 9h). Samples from groups 3 and 4 showed two inflection points in M_{RS} (Figures 9a, 9d, 9i, 9m, 9n, and 9p), consistent with the two distinct Curie points identified on the $M_S(T)$ curves (Figures 5a, 5d, 5i, 5m, 5n, and 5p). Despite this agreement between continuous $M_S(T)$ and progressive $M_{RS}(T)$ curves, we could not identify any correlation between the linearity of the PCA fits and the rock-magnetic groups. For this collection of samples, we also could not identify any simple relationship between the coercivity spectra from AF demagnetizations (Figure 9, blue circles) and the temperature spectrum from TH demagnetizations (Figure 9, red squares).

Based on the good agreement between AF and TH demagnetization curves as well as the more gentle unblocking of magnetization by AF treatment, we chose to AF demagnetize the rest of the samples and to only rely on directions from AF demagnetization curves for our final statistics. For the whole collection of 1,024 samples, a secondary component of magnetization was generally removed by 10–20 mT whereas the ChRM component, fitted by principal component analysis above 20–30 mT, unidirectionally decayed toward the origin. After excluding four flows from Section 01 yielding erratic directions (precision parameter $k < 25$), we interpreted 812 of 945 AF demagnetization curves from 78 lava flows, leading to a median of 10 individual directions (IQR of 3) per flow. Fisher's statistics of the 78 flows are reported in Table 1 and Figures 10a and 10b. With the exception of Flow 40 from Section 04, the 95% confidence radius α_{95} does not exceed 10°, with a median of 4.3° (IQR of 1.8°). The precision parameter k exceeds 50 (resp. 100) in 95% (resp. 73%) of the cases. Flows 04, 18, 33 and 44 are the most scattered, with k ranging between 40 and 50. According to Vandamme (1994)'s trimming method yielding an optimal cutoff angle of 40.9°, only Flow 06 is marked as transitional. The VGP scatter of the remaining 77

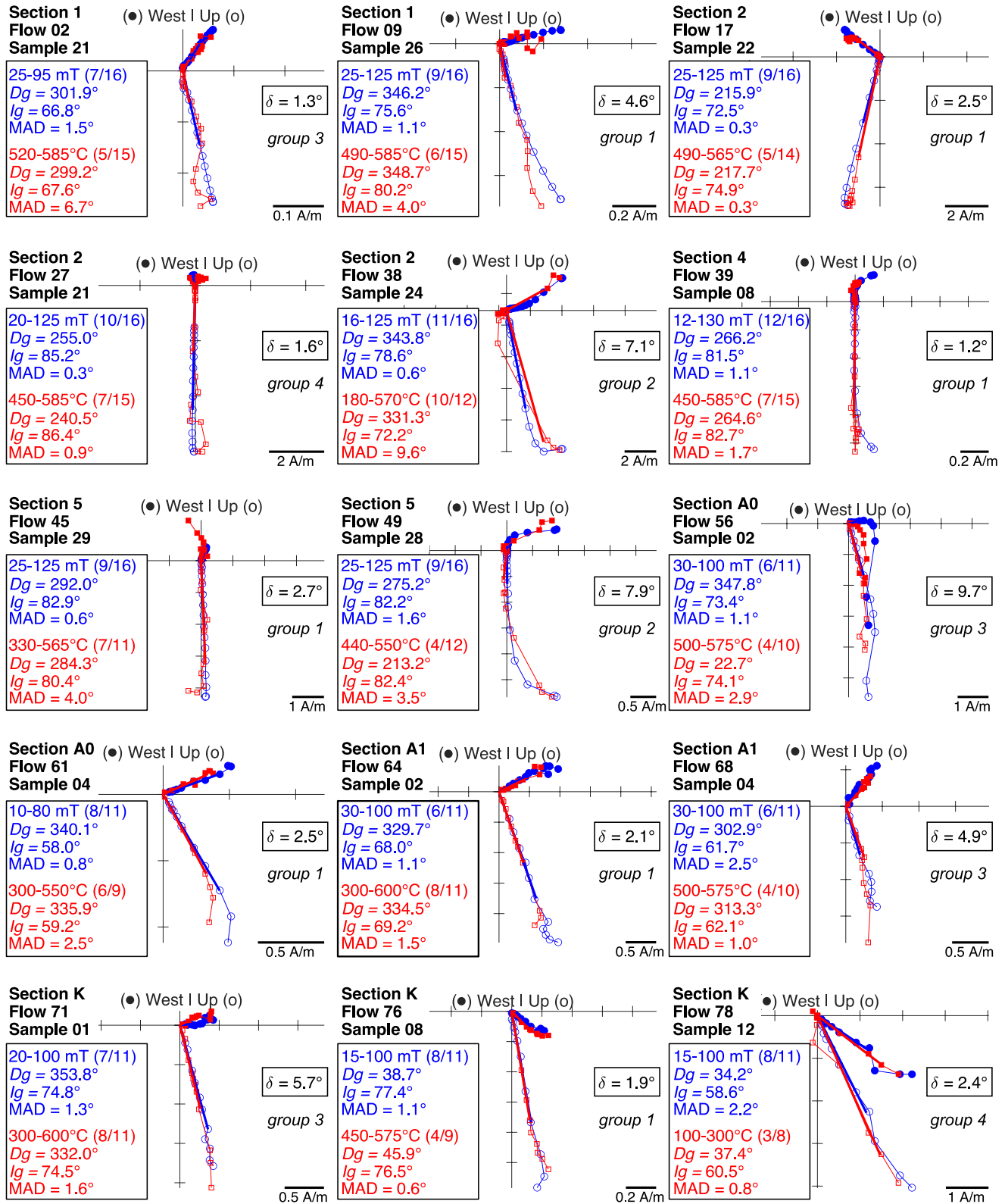


Figure 8. Vector endpoint diagrams showing alternating field (AF, blue circles) and thermal (TH, red squares) demagnetization curves for 15 representative samples from the same flows as in Figure 5. The insets provide the anchored directions (D_g , I_g) in geographic coordinates determined by principal component analysis, together with the maximum angular deviation and the angular distance (δ) between the directions obtained by AF and TH treatment.

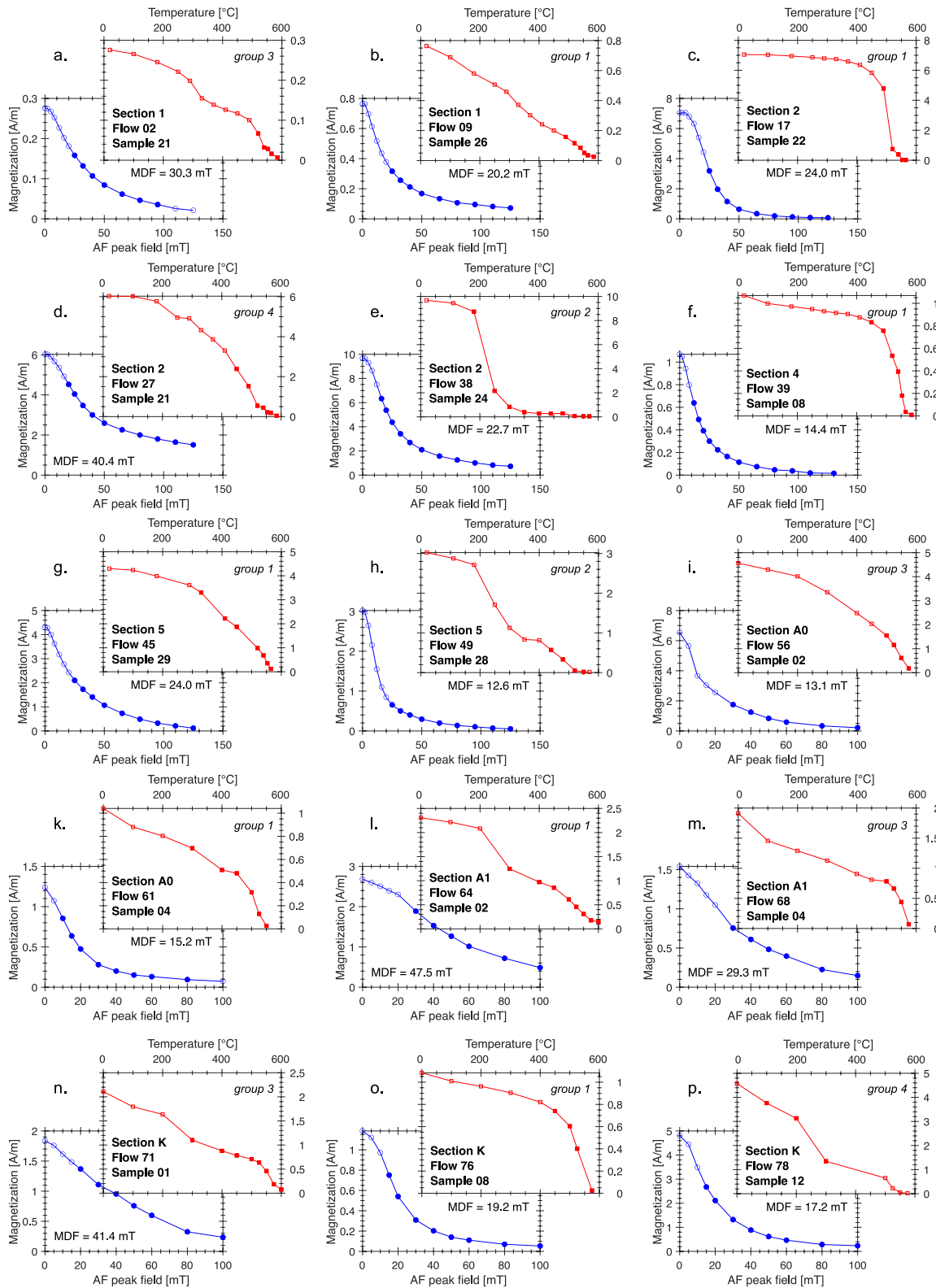


Figure 9. Demagnetization spectra for each pair of alternating field (AF, blue circles) and thermally (red squares) demagnetized specimens shown in Figure 8. The medium destructive field represents the value for which half of the NRM is randomized by AF demagnetization.

Table 1

Paleomagnetic Results of the 78 Lava Flows Interpreted in This Study: Site (or Group) Name; Number n of Interpreted Samples; Number N of Measured Samples; Declination (D_g) and Inclination (I_g) in Geographic Coordinates; Declination (D_s) and Inclination (I_s) in Stratigraphic Coordinates With Precision Parameter (k) and 95% Confidence Radius (α_{95}); Longitude (Plon) and Latitude (Plat) of the Virtual Geomagnetic Poles Calculated From Mean D_s and I_s

Site/group	n	N	D_g	I_g	D_s	I_s	k	α_{95}	Plon	Plat
Section 1 (66.9°N 169.8°E)—strike 80°, dip 3°										
Flow 01 (010101)	10	11	229.2	85.7	205.4	83.6	213.3	3.3	160.4	55.1
Flow 02 (010404)	23	25	290.8	72.4	282.0	73.7	78.9	3.4	105.9	56.6
Flow 03 (010507)	6	11	339.6	80.2	335.1	83.1	61.6	8.6	141.6	77.9
Flow 04 (010605)	11	17	275.4	75.2	264.0	75.7	44.6	6.9	120.8	53.2
Flow 05 (010808)	10	10	357.4	66.6	358.4	69.6	117.8	4.5	353.9	76.4
Flow 06 (010912)	9	11	4.4	53.0	5.5	55.9	83.6	5.7	341.1	59.4
Flow 07 (011018)	10	10	346.7	74.7	345.9	77.7	103.6	4.8	81.6	84.4
Flow 08 (011113)	15	19	324.1	71.8	319.4	74.4	62.1	4.9	80.2	71.5
Flow 09 (011219)	8	11	338.6	82.1	331.8	85.0	130.8	4.9	151.5	74.9
Flow 10 (011309)	12	17	358.9	70.6	0.5	73.6	137.8	3.7	347.8	82.6
Flow 11 (011410)	5	8	303.6	76.9	292.6	78.8	165.5	6.0	114.4	65.6
Flow 12 (011520)	7	12	333.8	74.8	330.0	77.7	690.6	2.3	91.5	78.2
Flow 13 (011611)	12	13	57.4	86.8	110.9	86.6	66.2	5.4	184.2	63.8
Flow 14 (011714)	16	19	26.7	74.4	34.3	76.7	157.4	2.9	252.7	76.0
Flow 15 (011815)	8	18	48.4	73.4	57.8	74.8	213.1	3.8	244.5	65.2
Flow 16 (011916)	12	12	47.9	79.7	64.0	80.9	100.6	4.3	217.4	68.2
Flow Mean (Section 1)	16		347.2	78.1	346.2	81.1	42.5	5.7	139.7	81.7
Section 2 (66.9°N 169.9°E)—strike 70°, dip 5°										
Flow 17 (020101)	15	22	195.3	79.5	184.2	75.1	157.4	3.1	167.4	38.9
Flow 18 (020203)*	12	12	5.2	75.8	17.4	80.1	47.8	6.3	220.4	82.7
Flow 19 (020302)*	17	22	33.3	74.7	51.0	77.1	100.6	3.6	240.2	69.9
Flow 20 (020417)*	10	10	14.4	79.4	37.8	82.9	104.2	4.8	205.8	75.3
Flow 21 (020506)*	11	17	13.4	76.4	29.4	80.2	201.3	3.2	225.6	78.8
Flow 22 (020605)*	11	17	10.3	75.9	24.5	79.9	195.1	3.3	227.4	80.5
Flow 23 (020704)*	11	18	10.9	75.9	25.3	79.9	77.0	5.2	227.6	80.2
DG 01 (18–23)	72				33.3	80.0	89.4	1.8	227.9	77.6
Flow 24 (020818)*	12	12	14.8	82.9	58.3	85.9	81.7	4.8	190.6	70.0
Flow 25 (020919)*	10	10	357.4	76.9	7.4	81.5	106.5	4.7	187.7	83.1
Flow 26 (021020)*	12	12	14.9	83.8	68.5	86.5	195.3	3.1	187.9	68.5
Flow 27 (021110)*	10	10	350.8	83.6	22.9	88.2	180.4	3.6	174.0	70.2
DG 02 (24–27)	44				35.4	86.1	110.7	2.1	185.1	72.7
Flow 28 (021209)	10	10	296.7	87	196.2	86.5	73.3	5.7	166.0	60.1
Flow 29 (021307)	11	14	76.5	83.1	110.0	81.0	67.1	5.6	201.1	56.8
Flow 30 (021408)	16	17	39.2	68.8	51.6	70.9	226.8	2.5	260.2	63.5
Flow 31 (021511)	18	20	55.6	73.8	73.1	74.3	256.4	2.2	235.7	59.1
Flow 32 (021612)	9	9	28.8	69.4	40.6	72.3	148.3	4.2	267.2	69.3
Flow 33 (021713)*	18	22	39.5	82.3	79.2	83.3	49.5	5.0	203.2	65.8
Flow 34 (021814)*	16	19	65.3	83.4	104	82.1	210.5	2.5	200.6	59.4
DG 03 (33–34)	34				92.0	82.9	76.9	2.8	201.8	62.8
Flow 35 (021915)	8	8	302.3	76.1	285.5	79.6	84.4	6.1	120.4	64.1

Table 1
Continued

Site/group	<i>n</i>	<i>N</i>	<i>D_g</i>	<i>I_g</i>	<i>D_s</i>	<i>I_s</i>	<i>k</i>	α_{95}	Plon	Plat
Flow 36 (022022)	10	10	27.0	72.9	41.6	75.8	163.5	3.8	252.4	72.4
Flow 37 (022121)	9	9	48.1	80.3	78.5	80.9	148.4	4.2	213.2	64.1
Flow 38 (022216)	19	20	320.4	85.6	219.9	88.3	60.5	4.3	164.9	64.2
Flow Mean (Section 2)	22		20.8	80.8	51.8	83.7	87.1	3.3	202.1	71.9
DG Mean (Section 2)	13				64.3	84.0	59.4	5.4	200.3	69.2
Section 4 (67.0°N 170.3°E)—strike 59°, dip 6°										
Flow 39 (040101)	17	19	265.7	79.2	232.5	80.3	372.0	1.9	145.3	52.6
Flow 40 (040302)*	5	10	38.9	71.6	57.3	72.7	41.8	12.0	251.5	63.2
Flow 41 (040403)*	10	10	28.1	74.4	50.0	76.5	129.9	4.3	244.1	69.8
Flow 42 (040504)*	6	8	49.2	76.7	74.5	76.4	309.3	3.8	230.1	60.9
DG 04 (40–42)	21				58.7	75.8	95.7	3.3	241.3	65.9
Flow Mean (Section 4)	4		26.8	79.8	62.6	81.4	42.3	14.3	214.7	69.0
DG Mean (Section 4)	2				71.9	87.7			181.0	67.8
Section 5 (66.9°N 170.1°E)—strike 27°, dip 5° (43–47); strike 80°, dip 9° (48); strike 56°, dip 4° (49–54)										
Flow 43 (050104)*	10	10	308.6	80.9	330.9	85.2	515.9	2.1	152.5	74.6
Flow 44 (050203)*	9	10	311.9	79.3	330.6	83.5	199.3	3.7	142.0	76.6
DG 05 (43–44)	19				330.9	84.4	301.2	1.9	148.0	75.6
Flow 45 (050302)	10	10	285.4	80.0	283.8	85.0	201.2	3.4	144.5	67.2
Flow 46 (050405)*	7	9	342.1	88.6	91.7	85.6	139.1	5.1	191.3	65.1
Flow 47 (050501)*	7	8	189.7	88.1	126.8	84.4	162.7	4.7	187.5	59.0
DG 06 (46–47)	14				111.9	85.3	151.8	3.2	188.9	62.1
Flow 48 (050606)	11	11	203.9	87.2	177.9	78.6	235.6	3.0	171.2	44.9
Flow 49 (050707)	10	11	250.6	77.6	232.1	78.0	180.5	3.6	142.2	48.8
Flow 50 (050808)	11	11	273.0	81.9	243.9	83.5	115.1	4.3	147.2	59.1
Flow 51 (050909)*	7	8	315.6	83.8	298.0	87.6	473.3	2.8	158.4	68.7
Flow 52 (051010)*	8	10	303.7	86.5	206.2	88.5	192.7	4.0	167.1	64.2
Flow 53 (051111)*	10	10	259.5	85.8	205.0	85.5	315.5	2.7	162.9	58.6
Flow 54 (051212)*	11	11	295.4	87.1	190.5	87.9	126.0	4.1	168.4	62.8
DG 07 (51–54)	36				212.1	87.8	197.4	1.7	164.9	63.1
Flow Mean (Section 5)	12		284.4	84.8	226.5	87.5	173.6	3.3	162.2	63.4
DG Mean (Section 5)	7				225.2	86.1	134.3	5.2	158.8	61.1
Section A0 (66.9°N 170.2°E)—strike 56°, dip: 6°										
Flow 55 (A0120)	6	7	358.6	73.3	13.7	77.9	103.4	6.6	255.0	84.6
Flow 56 (A0219)	7	9	313.7	81.7	286.1	87.2	302.8	3.5	155.9	67.8
Flow 57 (A0318)*	7	7	259.3	78.2	229.4	79.1	101.3	6.0	145.1	50.0
Flow 58 (A0417)*	9	9	288.6	81.3	246.0	84.6	368.2	2.7	149.7	60.9
DG 08 (57–58)	16				235.7	82.3	146.5	3.1	147.4	56.1
Flow 59 (A0516)	8	8	338.7	69.2	343.6	75.0	231.3	3.6	52.2	81.3
Flow 60 (A0615)	8	8	267.1	74.0	245.9	76.1	111.0	5.3	132.2	48.9
Flow 61 (A0713)	9	9	331.2	62.9	332.6	68.9	352.3	2.7	46.4	70.2
Flow 62 (A0811)	6	10	310.3	63.6	306.1	69.3	96.5	6.9	78.6	60.8
Flow 63 (A0912)	8	8	322.3	83.0	301.4	88.9	133.6	4.8	165.2	68.0
Flow Mean (Section A0)	9		315.1	76.2	307.0	82.0	51.9	7.2	128.9	71.4

Table 1
Continued

Site/group	<i>n</i>	<i>N</i>	<i>D_g</i>	<i>I_g</i>	<i>D_s</i>	<i>I_s</i>	<i>k</i>	α_{95}	Plon	Plat
DG Mean (Section A0)	8				313.7	81.2	51.7	7.8	124.3	73.3
Section A1 (66.9°N 170.4°E)—strike 13°, dip: 12°										
Flow 64 (A1004)	11	11	330.8	80.6	52.0	81.0	82.0	5.1	219.9	71.8
Flow 65 (A1105)	11	11	326.8	72.8	10.2	78.2	124.8	4.1	249.6	86
Flow 66 (A1206)	9	10	303.7	73.4	341.4	83.2	118.0	4.8	148.0	78.8
Flow 67 (A1307)	10	11	328.0	64.6	353.3	71.2	114.8	4.5	9.5	78.4
Flow 68 (A1408)*	9	9	293.3	78.7	36.6	87.8	51.8	7.2	178.2	70.3
Flow 69 (A1509)*	9	9	262.6	75.1	214.2	84.5	253.0	3.2	159	57.3
Flow 70 (A1610)*	9	12	284.0	71.8	285.9	83.8	86.9	5.6	138.6	67.2
<i>DG 09 (68–70)</i>	27				261.9	87.4	74.3	3.2	157.9	65.7
Flow Mean (Section A1)	7		305.5	75.2	355.9	84.1	87.9	6.5	166.3	78
DG Mean (Section A1)	5				3.1	81.6	96.1	78	177.6	82
Section K (66.8°N 169.8°E)—strike 0°, dip 3° (71–74); dip 0° (75–78)										
Flow 71 (K00108)*	10	12	0.2	71.4	9.0	71.2	110.9	4.6	324.4	78.2
Flow 72 (K00207)*	12	12	357.3	67.4	4.5	67.4	139.2	3.7	339.8	73.3
<i>DG 10 (71–72)</i>	22				6.4	69.1	120.7	2.8	334.1	75.5
Flow 73 (K00306)*	11	12	92.9	89.1	90.7	86.1	85.9	5.0	188.8	65.5
Flow 74 (K00405)*	12	12	28.3	86.2	55.1	84.1	218.4	2.9	200.5	71.0
<i>DG 11 (73–74)</i>	23				68.3	85.3	124.0	2.7	194.1	68.5
Flow 75 (K00501)	8	10	160.7	84.2	160.7	84.2	145.9	4.6	176.5	55.8
Flow 76 (K00602)	9	9	35.6	67.5	35.6	67.5	218.8	3.5	284.8	65.8
Flow 77 (K00703)	9	10	4.5	79.5	4.5	79.5	394.8	2.6	198.0	86.7
Flow 78 (K00804)	7	10	20	71.8	20	71.8	57.0	8.1	297.5	76.3
Flow Mean (Section K)	8		15.7	79	22.8	78.4	55.1	7.5	235.4	80.9
DG Mean (Section K)	6				24.6	78.4	51.4	9.4	236.0	80.4
Flow Mean (all study)	78		346.3	81.3	8.7	85.0	53.5	2.2	176.1	76.0
DG Mean (all study)	57				0.4	84.6	46.2	2.8	170.0	76.8

Note. Flows marked with an asterisk (*) were merged into directional groups (DG) highlighted in italics.

stable directions, corrected for within-site dispersion, is $S_b = 19.4^\circ_{17.6^\circ}^{21.4^\circ}$. We note that (a) removing the sites with higher dispersion ($k \leq 100$ or $k \leq 50$) yields statistically indistinguishable estimates of the VGP scatter, and (b) the cutoff method of the VGPs has little influence on the final results (Table 2).

Using the algorithm proposed by Chenet et al. (2008), serial correlations were found for 32 flows, leading to the creation of 11 DG (Table 1; Figure 10c). Our preferred data set thus relies on 57 paleomagnetic directions (46 individual flows + 11 DG) thought to represent snapshots of the paleomagnetic field. With an optimal cutoff angle of 44.4° or a fixed cutoff of 45°, no transitional direction is detected; Flow 06 is not marked as transitional anymore. The VGP position is 170.0°E, 76.8°N ($N = 57$, $K = 14$, $A_{95} = 5.2^\circ$), with an angular standard deviation $S_b = 21.5^\circ_{19.3^\circ}^{24.0^\circ}$. Once more, removing the sites with $k \leq 100$ or $k \leq 50$ has little influence on S_b (Table 2).

As the directions were emplaced at the end of the CNS, a reversal test cannot be employed to ascertain the robustness of the remanence. A fold test has a limited scope for the present collection due to the small variations in the lava's bedding (dip $\leq 12^\circ$; Table 1). However, we note that a bootstrap fold test (Figures 10d and 10e; Tauxe & Watson, 1994) or a DC fold test (Enkin, 2003), applied to the individual flows or DGs, is not inconsistent with a pre-folding age of the isolated ChRM component. As a corollary, a positive fold test also corroborates our geological observations according to which the dips of the lava flows are the result of post-emplacment tectonics rather than of the emplacement of the lava flows on an initially tilted surface.

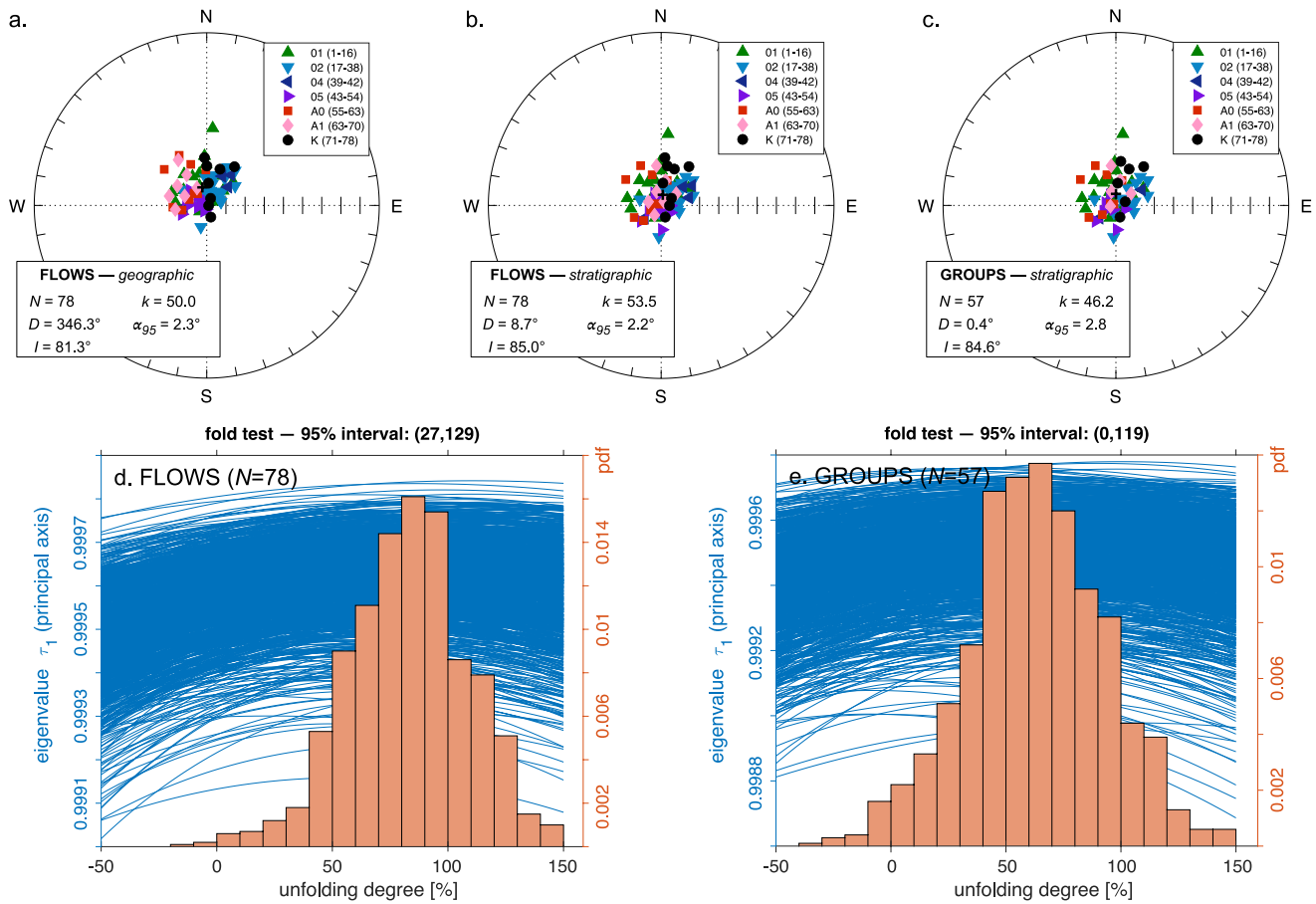


Figure 10. Average paleodirections from this study. (a, b) Equal-area projection of the flow-mean directions in geographic and stratigraphic coordinates. (c) Equal-area projection of the directional groups after considering the serial correlations of the flows. (d, e) Bootstrap fold test before (panel d) and after (panel e) considering the serial correlations. Trend of the largest eigenvalue τ_1 of the orientation matrix from 1,000 representative pseudo-samples (left axis, blue lines); probability density function of the 1,000 maxima of τ_1 (right axis, red histograms).

Table 2
Virtual Geomagnetic Pole Scatter, Corrected for Within-Site Dispersion, for Various Filtering Scenarios

	No cutoff (or 45° cutoff)				Vandamme cutoff				
	<i>N</i>	<i>S_b</i>	<i>S_b⁻</i>	<i>S_b⁺</i>	<i>N</i>	<i>A</i>	<i>S_b</i>	<i>S_b⁻</i>	<i>S_b⁺</i>
Flows, all	78	19.9	18.0	22.2	77	40.9	19.4	17.6	21.4
<i>k</i> > 50	74	19.9	17.9	22.2	73	40.7	19.3	17.5	21.3
<i>k</i> > 100	57	19.8	17.7	22.0	57	41.2	19.8	17.7	22.0
Groups, all	57	21.5	19.3	24.0	57	44.4	21.5	19.3	24.0
<i>k</i> > 50	56	21.3	19.1	23.9	56	44.1	21.3	19.1	23.9
<i>k</i> > 100	40	21.2	18.8	23.9	40	43.7	21.2	18.7	23.8

Note. The angular standard deviation S_b is provided with its 95% confidence interval [S_b^- ; S_b^+] computed from 100,000 bootstrapped samples. The quantity *A* is the optimum cutoff angle when Vandamme (1994)'s trimming method is applied. The bold values correspond to our preferred scenario when serially-correlated flows are grouped according to Chenet et al. (2008)'s method. No transitional flows/groups are detected in this scenario.

5. Discussion

5.1. Robustness of the Data Set for PSV Analysis

We investigated seven suites of lava flows within an area of 400 km² in the vicinity of the Kupol ore deposit (Bilibinsky District, Chukotka). From 82 investigated flows, 78 yielded reliable paleodirections, with a ChRM component mainly carried by titanomagnetite grains. Due to the existence of serially-correlated flows within the sequences, our final data set rely on 57 paleodirectional snapshots. Based on stratigraphic constraints, Section A1 (mapped in the uppermost volcanic units; Figure 2) and Section A0 (mapped in the Kovalenko suite; Figure 2) can be claimed to be younger and thus independent in time from the five other sections (mapped in the Kayemravaam suite; Figure 2). Based on radioisotopic constraints, Section 1 can be claimed to be older than Section 4 due to discordant U-Pb ages (Section 4.1). Even if we cannot completely exclude partial overlaps between Sections 1, 2, 5, and K, our field observations indicate that they have different stratigraphic positions within the Kayemravaam suite. Additionally, we could not identify obvious overlaps in the magnetostratigraphy of these four sections. We consequently claim that the seven sections are independent in time and that our paleodirectional data set represents 57 time-independent horizons of the paleomagnetic field at the end of the CNS.

Table 3

Comparison of Paleomagnetic Poles for North-Eastern Eurasia: Pole Longitude (Plon), Pole Latitude (Plat), Number *N* of Individual Virtual Geomagnetic Poles, and 95% Confidence Radius (A_{95})

Reference	Region	Age (Ma)	Plon (°E)	Plat (°N)	<i>N</i>	A_{95}
This study	Chukotka	84–89	170.0	76.8	57	5.2
Torsvik et al. (2012) ^a	Laurentia	80	194.6	74.4	7	7.0
Torsvik et al. (2012) ^a	Laurentia	90	198.6	74.7	4	6.3
Torsvik et al. (2012) ^a	Baltica-Siberia	80	153.2	72.3	4	3.0
Torsvik et al. (2012) ^a	Baltica-Siberia	90	158.1	73.4	4	6.2
Metelkin et al. (2007)	South Siberia	74–82	185.5	82.8	16	6.1
Otofujii et al. (2015) ^b	see below	~80	164.7	68.0	12	10.9
Lebedev et al. (2021)	Chukotka	~85	183.7	69.4	60	6.1

^aRunning mean. ^bCombined pole from the Kolyma-Omolon terrane (Otofujii et al., 2015) and the Chukotka terrane (Stone et al., 2009).

We note that our new paleomagnetic pole is located in close proximity to the nearly coeval paleomagnetic poles previously obtained in this region (Table 3; Lebedev et al., 2021; Otofujii et al., 2015; Stone et al., 2009). Our pole also lies in a short distance from the only reliable Late Cretaceous paleomagnetic pole of Siberia (Table 3; Metelkin et al., 2007) as well as from the apparent polar wander path of Laurentia and Baltica-Siberia between 80 and 90 Ma (Table 3; Torsvik et al., 2012), noting that Chukotka is currently considered to belong to the North American tectonic plate (Gaina et al., 2002). Taken together, these observations tend to support the primary origin of the isolated ChRM and this data set thus provides a solid base for the analysis of PSV.

5.2. Latitudinal Dependency of the VGP Scatter During the CNS

To analyze the paleolatitudinal dependency of the VGP scatter S_b during the CNS (conservatively defined as polarity chron C34n; Ogg, 2020), we relied on the recent compilation of S_b estimates calculated by Doubrovine et al. (2019) from various paleodirectional data sets determined from rapidly-cooled igneous units. We added to this compilation the new estimate $S_b = 12.0^\circ |_{10.3^\circ}^{13.7^\circ}$ ($N = 44$, with Vandamme cutoff) or $S_b = 16.7^\circ |_{13.6^\circ}^{21.2^\circ}$ ($N = 49$, with 45° cutoff) from the Ramon volcanics (southern Israel) emplaced in the beginning of the CNS (112.6–119 Ma) at low paleolatitude (Dembo et al., 2022), as well as our estimate $S_b = 21.5^\circ |_{19.3^\circ}^{24.0^\circ}$ ($N = 57$, no transitional directions) from the OCVB (north-eastern Russia) emplaced in the end of CNS (84–89 Ma) at high paleolatitude (Figures 11a and 11b). We note that our new estimate from the OCVB is in excellent agreement with the estimate $S_b = 20.8^\circ |_{17.5^\circ}^{23.7^\circ}$ ($N = 37$, no transitional directions) from the Arctic Canadian Volcanics, also emplaced in the end of the CNS (95.1–95.5 Ma) at high paleolatitude (Tarduno et al., 2002).

Considering the data sets of stable VGPs trimmed with the 45° or Vandamme cutoff procedure, we fitted the paleolatitudinal dependency $S_b^2(\lambda) = a^2 + (b\lambda)^2$ by model G of McFadden et al. (1988) for various filtering scenarios in terms of the number N of stable VGPs per study (Figures 11a and 11b; Table 4). To this end, we used a linear least-square regression, wherein the observations S_b^2 were weighted by the inverse of the relative standard deviation $\sigma(S_b^2) = 2\sigma(S_b) \cdot S_b$ and the 95% confidence interval on (a, b) was derived from the least-square covariance matrix. Consistent with previous analyses of (a, b) during the CNS (e.g., Biggin et al., 2008; Doubrovine et al., 2019), the uncertainties on (a, b) are usually 10%–50% smaller for the data sets trimmed with the Vandamme cutoff than for those trimmed with the 45° cutoff, provided that the number N_{fd} of fitted data exceeds five (Table 4). This a posteriori confirms that the Vandamme cutoff procedure is more appropriate to isolate stable VPGs than the 45° cutoff procedure that does not account for the paleolatitudinal dependency of PSV. Generally, the a -values (resp. b -values) are 20%–25% higher (resp. 5%–10% lower) for strict selection criteria ($N \geq 40$) than for lenient selection criteria ($N \geq 10$). However, we cannot interpret these changes as robust features due to the low number of available studies ($N_{fd} \leq 5$) fulfilling strict selection criteria. To keep the relative uncertainties of (a, b) below 25%, we considered the intermediate filtering scenario ($N \geq 20$) as the best comprise to interpret the paleolatitudinal dependency of S_b . In this latter case, the values $a = 9.4 \pm 2.3$ and $b = 0.23 \pm 0.06$ ($N_{fd} = 11$) are consistent, to within the uncertainties, with the values obtained by Doubrovine et al. (2019) for the CNS (Table 4). Compared to the PCRS (Handford et al., 2021), the equatorial value a would

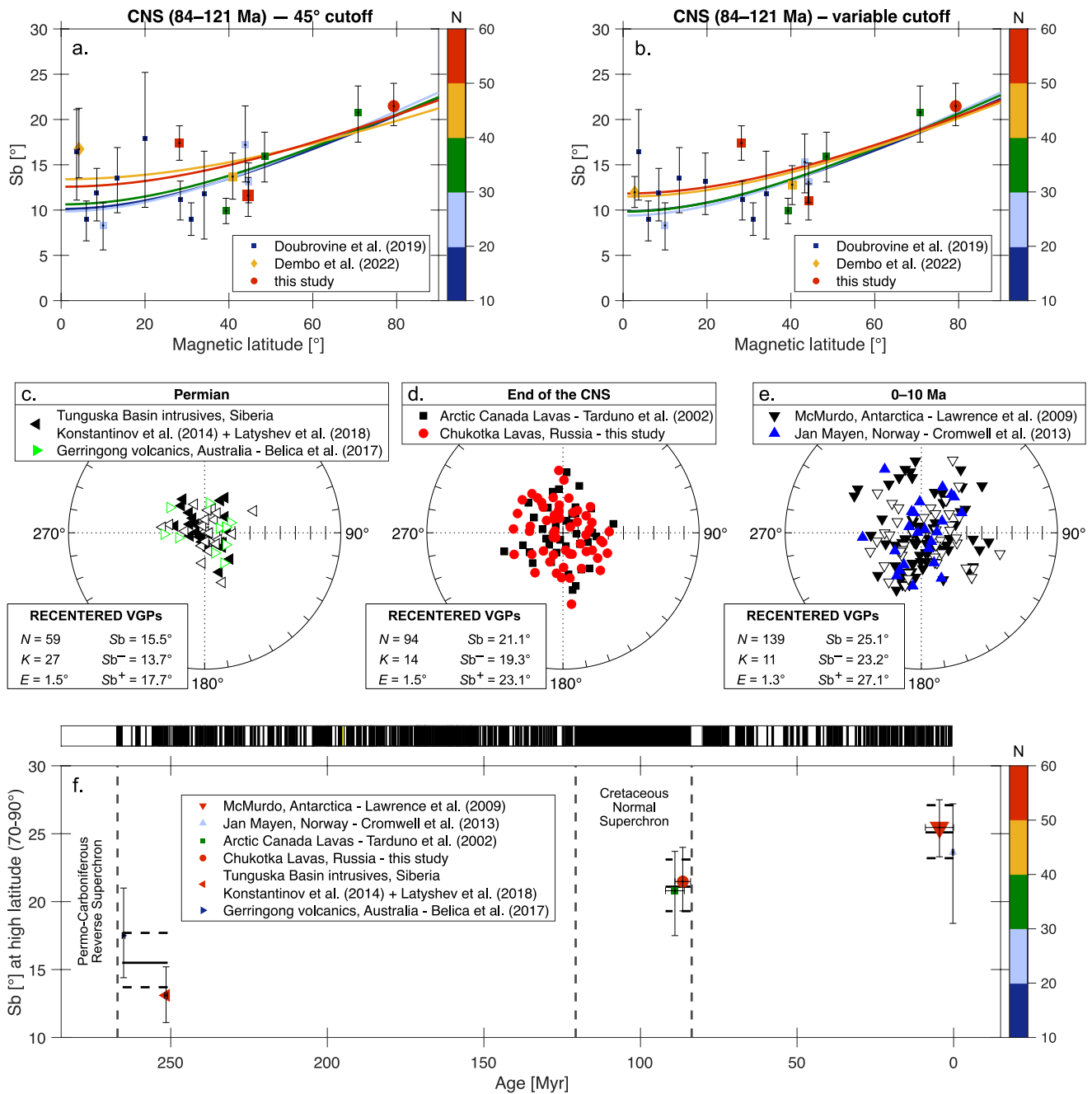


Figure 11. Spatio-temporal evolution of the virtual geomagnetic pole (VGP) scatter S_b . (a, b) Latitudinal profile of S_b during the Cretaceous Normal Superchron (CNS), defined as polarity chron C34n; Ogg, 2020) when employing a 45° cutoff (panel a) or a variable cutoff (panel b; Vandamme, 1994) of the VGPs to remove presumably transitional directions. The S_b values are taken from the compilation of Doubrovine et al. (2019), supplemented by the new estimate at low latitude from the Ramon volcanics (Dembo et al., 2022) and our new estimate at high latitude. The color/size coding of the symbols represent the number N of stable directions used to compute S_b . (c–e) Equal-area projection of the recentered VGPs for identified collections of igneous units emplaced at high magnetic latitude (70–90°) during the Permian (panel c), the end of the CNS (panel d) and the past 10 Myr (panel e). (f) Time evolution of S_b values at high magnetic latitude (70–90°). Same color/size coding as in panels (a–c). The black horizontal lines represent the S_b estimates of the three combined data sets. The upper inset shows a composite geomagnetic polarity timescale: see Ogg (2020) for the C- and M-sequences; Hesselbo et al. (2020) for the Jurassic, Ogg et al. (2020) for the Triassic, Henderson et al. (2020) for the Permian.

be 20%–40% higher during the CNS whereas the latitudinal factor b would be 30%–40% smaller during the CNS (Table 4). To within the uncertainties, the latitudinal factor b during the CNS would be indistinguishable from the value for the past 10 Myr (de Oliveira et al., 2021) whereas the equatorial value a would be 30% lower during the CNS than during the past 10 Myr. Consistent with Doubrovine et al. (2019), our analysis thus tends to confirm

Table 4

Estimates of Parameters (a, b) of Model G During the Cretaceous Normal Superchron (CNS) for Various Filtering Scenarios in Terms of the Number N of Stable Virtual Geomagnetic Poles Per Individual Study, To Be Compared With Previous Estimates From the CNS (Doubrovine et al., 2019), the Permo-Carboniferous Reverse Superchron (Handford et al., 2021) and the Past 10 Myr (de Oliveira et al., 2021)

	45° cutoff			Vandamme cutoff		
	N_{fd}	a	b	N_{fd}	a	b
CNS (84–121 Ma), $N \geq 10^a$	19	10.1 ± 2.5	0.22 ± 0.06	19	9.9 ± 2.1	0.22 ± 0.05
CNS (84–121 Ma), $N \geq 20^a$	11	9.9 ± 3.3	0.23 ± 0.08	11	9.4 ± 2.3	0.23 ± 0.06
CNS (84–121 Ma), $N \geq 30^a$	8	10.6 ± 5.7	0.22 ± 0.10	8	9.8 ± 4.9	0.23 ± 0.09
CNS (84–121 Ma), $N \geq 40^a$	5	13.4 ± 5.7	0.18 ± 0.15	5	11.5 ± 5.2	0.21 ± 0.12
CNS (84–121 Ma), $N \geq 50^a$	3	12.6 ± 12.1	0.20 ± 0.23	3	11.8 ± 13.8	0.21 ± 0.24
CNS (84–126 Ma), $N \geq 10^b$	19	$11.1^{+2.6}_{-2.6}$	$0.21^{+0.19}_{-0.06}$	19	$10.7^{+2.4}_{-2.2}$	$0.21^{+0.16}_{-0.05}$
CNS (84–126 Ma), $N \geq 20^b$	11	$8.2^{+4.6}_{-5.6}$	$0.27^{+0.14}_{-0.05}$	11	$8.1^{+4.7}_{-5.4}$	$0.26^{+0.16}_{-0.04}$
PCRS (265–318 Ma), Group 1 ^c	n/a	n/a	n/a	16	$5.5^{+4.7}_{-3.1}$	$0.33^{+0.09}_{-0.09}$
PCRS (265–318 Ma), Group 2 ^c	n/a	n/a	n/a	12	$7.2^{+5.2}_{-3.4}$	$0.30^{+0.13}_{-0.12}$
0–10 Ma ^d	75	$13.2^{+1.4}_{-1.3}$	$0.23^{+0.05}_{-0.05}$	70	$12.4^{+1.5}_{-1.3}$	$0.23^{+0.05}_{-0.04}$

Note. The quantity N_{fd} correspond to the number of fitted data.

^aThis study. ^bDoubrovine et al. (2019). ^cHandford et al. (2021). ^dde Oliveira et al. (2021).

the existence of a latitudinal dependency of S_b similar to that observed for the past 10 Myr. Nevertheless, due to the large uncertainties in the parameters as well as the discrepancies arising from using different filtering and/or fitting procedures, we think that quantitatively interpreting the temporal changes of the latitudinal profile of S_b remains a challenging task.

5.3. Temporal Comparison of the VGP Scatter at High Latitude

By scanning the recent PSV databases for the past 10 Myr (Cromwell et al., 2018; de Oliveira et al., 2021), the Miocene (Engbers et al., 2022), the Jurassic-Cretaceous (Doubrovine et al., 2019) and the Permo-Triassic (Handford et al., 2021), we identified five data sets, in addition to the present one from the OCVB, that were emplaced at a magnetic paleolatitude greater than 70°. First, the lava flows from the Erebus Volcanic Province in Antarctica (Lawrence et al., 2009) and those from the Jan Mayen island in the Norwegian Arctic (Cromwell et al., 2013) provides a characterization of the geomagnetic field for the past 10 Myr. Second, the lava flows from the Strand Fiord Formation in the Canadian Arctic (Tarduno et al., 2002) and those from the OCVB (this study) quantify PSV at the end of the CNS. Finally, the Gerringong volcanics from West Australia (Belica et al., 2017) and the intrusives from the Tunguska Basin in Siberia (Konstantinov et al., 2014; Latyshev et al., 2018) characterize the paleomagnetic field over a 15 Myr interval following the end of the PCRS, with the reservation that the intrusives from the Tunguska basin may not have averaged out PSV (Konstantinov et al., 2014). To produce an average estimate of PSV for each of the three time intervals, we first applied for each study the Vandamme cutoff procedure to remove potentially transitional directions. Second, we recentered for each study the distribution of stable VGPs around its principal axis. Third, we computed for each time interval the statistics of the combined recentered distributions (Figures 11c–11e).

We obtained for the combined data set at the end of the CNS $S_b = 21.1^\circ |^{23.1^\circ}_{19.3^\circ}$ ($N = 94$), to be compared with $S_b = 25.1^\circ |^{27.1^\circ}_{23.2^\circ}$ ($N = 139$) for the past 10 Myr and $S_b = 15.5^\circ |^{17.7^\circ}_{13.7^\circ}$ ($N = 59$) for the 250–265 Ma interval (Figure 11c). Comparing the 95% confidence intervals, we can reject, at 5% significance level, the null hypothesis according to which the populations for the 0–10 Ma and 84–92 Ma intervals would share the same S_b value (Figures 11d–11f). This indicates that the ~15% lower VGP scatter measured at high latitude at the end of CNS may be a robust feature, in agreement with Tarduno et al. (2002) and corroborating the trend predicted by numerical dynamo simulations (e.g., Aubert et al., 2010; Lhuillier & Gilder, 2013). Generally, the geomagnetic field may have experienced some variability in the amplitude of PSV during the CNS (e.g., Granot et al., 2012; Lhuillier et al., 2016) and/or brief events of reversed polarity at the beginning (e.g., Gale et al., 2020; Tarduno, 1990;

Tarduno et al., 1992) or at the end of CNS (He et al., 2012; Wang et al., 2016; Wu et al., 2013). Assuming that the 84–92 Ma interval may constitute a gradual transition toward a reversing regime of the geodynamo, it is not impossible that S_b at high latitude was still lower at times during the CNS.

Based on the comparison of the 95% confidence intervals, S_b at 250–265 Ma is statistically distinct from S_b at 0–10 Ma or 84–92 Ma (Figures 11c, 11d, and 11f). The low value of S_b should nevertheless be interpreted with caution. First, the S_b value from the Australian and Siberian data sets are largely discordant. Second, S_b from the Australian data set is only determined from 11 volcanic units, which may not be sufficient to provide a converged estimate. Third, paleodirections from the Tunguska basin are derived from intrusive rocks, which are not the ideal objects to determine S_b in the sense that each intrusion does not provide an instantaneous but a smoothed reading of the paleomagnetic field. Taken together, these observations likely point to an underestimation of S_b for the 250–265 Ma interval.

6. Conclusions

We investigated the paleomagnetism of a collection of 82 lava flows, dated 84–89 Ma, from the OCVB (NE Russia), yielding after removing erratic directions and combining serially-correlated directions:

1. a study-mean direction at $D = 0.4^\circ$, $I = 84.6^\circ$ ($\alpha_{95} = 2.8^\circ$, $N = 57$), indicative of an emplacement of the volcanics at a paleolatitude of $\sim 80^\circ\text{N}$;
2. a study-mean paleomagnetic pole located at 170.0°E , 76.8°N ($A_{95} = 5.2^\circ$, $N = 57$), in good agreement with previous estimates for north-eastern Eurasia;
3. a robust estimate of the VGP scatter, $S_b = 21.5^\circ|_{19.3^\circ}^{24.0^\circ}$ ($N = 57$), suitable for characterizing PSV at the end of the CNS.

Despite the heterogeneous magneto-mineralogy observed in terms of Curie points and hysteresis properties, we could not identify any correlation between the investigated rock-magnetic parameters and the directional statistics, which supports the robustness of the remanence record. Compared to previous PSV estimates published in the literature, we confirm that

4. VGP scatter is 2–2.5 times as high at the paleopole as at the paleoequator during the CNS;
5. VGP scatter at high paleolatitude (70° – 90°) is $\sim 15\%$ lower at the end of the CNS than during the past 10 Myr.

This latter observation confirms a potential link between polarity and PSV regimes of the geodynamo.

Data Availability Statement

The demagnetization data and fitted directions are available in the MagIC database (Lhuillier, Lebedev, et al., 2023).

References

- Akinin, V. V., & Miller, E. L. (2011). Evolution of calc-alkaline magmas of the Okhotsk-Chukotka volcanic belt. *Petrology*, 19(3), 237–277. <https://doi.org/10.1134/S0869591111020020>
- Amato, J. M., Toro, J., Akinin, V. V., Hampton, B. A., Salmikov, A. S., & Tuchkova, M. I. (2015). Tectonic evolution of the Mesozoic South Anyui suture zone, eastern Russia: A critical component of paleogeographic reconstructions of the Arctic region. *Geosphere*, 11(5), 1530–1564. <https://doi.org/10.1130/ges01165.1>
- Aubert, J., Tarduno, J. A., & Johnson, C. L. (2010). Observations and models of the long-term evolution of Earth's magnetic field. *Space Science Reviews*, 155(1–4), 337–370. <https://doi.org/10.1007/s11214-010-9684-5>
- Belica, M. E., Tohver, E., Pisarevsky, S. A., Jourdan, F., Denyszyn, S., & George, A. D. (2017). Middle permian paleomagnetism of the Sydney basin, eastern Gondwana: Testing Pangea models and the timing of the end of the Kiaman Reverse superchron. *Tectonophysics*, 699, 178–198. <https://doi.org/10.1016/j.tecto.2016.12.029>
- Belyi, V. F. (1977). *Stratigraphy and structures of the Okhotsk-Chukotka volcanic belt*. Nauka.
- Biggin, A. J., van Hinsbergen, D. J. J., Langereis, C. G., Straathof, G. B., & Deenen, M. H. L. (2008). Geomagnetic secular variation in the Cretaceous normal superchron and in the Jurassic. *Physics of the Earth and Planetary Interiors*, 169(1–4), 3–19. <https://doi.org/10.1016/j.pepi.2008.07.004>
- Bobrovnikova, E. M., Lhuillier, F., Shcherbakov, V. P., Shcherbakova, V. V., Zhidkov, G. V., Lebedev, I. E., et al. (2022). High-latitude Paleointensities during the Cretaceous normal superchron from the Okhotsk-Chukotka volcanic belt. *Journal of Geophysical Research: Solid Earth*, 127(2), e2021JB023551. <https://doi.org/10.1029/2021jb023551>
- Chenet, A.-L., Fluteau, F., Courtillot, V., Gérard, M., & Subbarao, K. V. (2008). Determination of rapid Deccan eruptions across the Cretaceous-Tertiary boundary using paleomagnetic secular variation: Results from a 1200-m-thick section in the Mahabaleshwar escarpment. *Journal of Geophysical Research*, 113(B4), B04101. <https://doi.org/10.1029/2006JB004635>

Acknowledgments

FL was supported by the Deutsche Forschungsgemeinschaft (DFG, German Research Foundation)—Projektnummer 405632737 and 521315821. VEP, IEL and PLT acknowledge the financial support from the Russian Science Foundation (RSF)—Grant 23-17-00112. We are grateful to Vladimir Tselmovich for his valuable help and advice in microscopic observations and their interpretation, as well as to Lisa Bobrovnikova for her significant contribution to magnetic measurements. We thank Mark Dekkers and the AE for editorial handling; Huapei Wang and two anonymous reviewers for their constructive comments that helped improve the manuscript. Open Access funding enabled and organized by Projekt DEAL.

- Cole, J., Milner, D., & Spinks, K. (2005). Calderas and caldera structures: A review. *Earth-Science Reviews*, 69(1–2), 1–26. <https://doi.org/10.1016/j.earscirev.2004.06.004>
- Cox, A. V. (1968). Lengths of geomagnetic polarity intervals. *Journal of Geophysical Research*, 73(10), 3247–3260. <https://doi.org/10.1029/JB073i010p03247>
- Cox, A. V. (1970). Latitude dependence of the angular dispersion of the geomagnetic field. *Geophysical Journal of the Royal Astronomical Society*, 20(3), 253–269. <https://doi.org/10.1111/j.1365-246X.1970.tb06069.x>
- Cromwell, G., Johnson, C. L., Tauxe, L., Constable, C. G., & Jarboe, N. A. (2018). PSV10: A global data set for 0–10 Ma time-averaged field and paleosecular variation studies. *Geochemistry, Geophysics, Geosystems*, 19(9), 839. <https://doi.org/10.1002/2017GC007318>
- Cromwell, G., Tauxe, L., Staudigel, H., Constable, C. G., Koppers, A. A. P., & Pedersen, R. B. (2013). In search of long-term hemispheric asymmetry in the geomagnetic field: Results from high northern latitudes. *Geochemistry, Geophysics, Geosystems*, 14(8), 3234–3249. <https://doi.org/10.1002/ggge.20174>
- Day, R., Fuller, M. D., & Schmidt, V. A. (1977). Hysteresis properties of titanomagnetites: Grain-size and compositional dependence. *Physics of the Earth and Planetary Interiors*, 13(4), 260–267. [https://doi.org/10.1016/0031-9201\(77\)90108-X](https://doi.org/10.1016/0031-9201(77)90108-X)
- Dembo, N., Kraus, E., Seliverstov, I., Weissman, G., & Granot, R. (2022). Geomagnetic field behaviour during the early Cretaceous normal superchron from palaeomagnetic analysis of the Ramon volcanics, Israel. *Geophysical Journal International*, 231(3), 1982–1995. <https://doi.org/10.1093/gji/ggac300>
- de Oliveira, W. P., Hartmann, G. A., Terra-Nova, F., Brandt, D., Biggin, A. J., Engbers, Y. A., et al. (2021). Paleosecular variation and the time-averaged geomagnetic field since 10 Ma. *Geochemistry, Geophysics, Geosystems*, 22(10), e2021GC010063. <https://doi.org/10.1029/2021gc010063>
- Di Chiara, A., Tauxe, L., Staudigel, H., Florindo, F., Protti, M., Yu, Y., et al. (2021). Earth's magnetic field strength and the Cretaceous normal superchron: New data from Costa Rica. *Geochemistry, Geophysics, Geosystems*, 22(4), e2020GC009605. <https://doi.org/10.1029/2020gc009605>
- Dodd, S. C., Muxworthy, A. R., & Mac Niocaill, C. (2015). Paleointensity determinations from the Etendeka province, Namibia, support a low-magnetic field strength leading up to the Cretaceous normal superchron. *Geochemistry, Geophysics, Geosystems*, 16(3), 785–797. <https://doi.org/10.1002/2014gc005707>
- Dobrovine, P. V., Veikkola, T., Pesonen, L. J., Piispa, E., Ots, S., Smirnov, A. V., et al. (2019). Latitude dependence of geomagnetic paleosecular variation and its relation to the frequency of magnetic reversals: Observations from the Cretaceous and Jurassic. *Geochemistry, Geophysics, Geosystems*, 20(3), 1240–1279. <https://doi.org/10.1029/2018GC007863>
- Driscoll, P. E., & Olson, P. L. (2009). Effects of buoyancy and rotation on the polarity reversal frequency of gravitationally driven numerical dynamos. *Geophysical Journal International*, 178(3), 1337–1350. <https://doi.org/10.1111/j.1365-246X.2009.04234.x>
- Duan, Z., Liu, Q., Ren, S., Li, L., Deng, X., & Liu, J. (2018). Magnetic reversal frequency in the lower Cambrian Niutitang formation, Hunan province, South China. *Geophysical Journal International*, 214(2), 1301–1312. <https://doi.org/10.1093/gji/ggy199>
- Dunlop, D. J. (2002). Theory and application of the Day plot (Mrs/Ms versus Hcr/Hc) 1. Theoretical curves and tests using titanomagnetite data. *Journal of Geophysical Research*, 107(B3), 2056. <https://doi.org/10.1029/2001JB000486>
- Eid, B., Lhuillier, F., Shcherbakov, V. P., & Shcherbakova, V. V. (2022). Do changes in geomagnetic secular variation, dipole moment and polarity reversal frequency correlate over the past 155 Myr? *Geophysical Journal International*, 230(2), 1132–1146. <https://doi.org/10.1093/gji/ggac112>
- Engbers, Y. A., Bono, R. K., & Biggin, A. J. (2022). PSVM: A global database for the Miocene indicating Elevated paleosecular variation relative to the last 10 Myrs. *Geochemistry, Geophysics, Geosystems*, 23(8), e2022GC010480. <https://doi.org/10.1029/2022gc010480>
- Enkin, R. J. (2003). The direction–correction tilt test: An all-purpose tilt/fold test for paleomagnetic studies. *Earth and Planetary Science Letters*, 212(1–2), 151–166. [https://doi.org/10.1016/S0012-821X\(03\)00238-3](https://doi.org/10.1016/S0012-821X(03)00238-3)
- Fabian, K., Shcherbakov, V. P., & McEnroe, S. A. (2013). Measuring the Curie temperature. *Geochemistry, Geophysics, Geosystems*, 14(4), 947–961. <https://doi.org/10.1029/2012GC004440>
- Fisher, R. (1953). Dispersion on a sphere. *Proceedings of the Royal Society of London Series A*, 217(1130), 295–305. <https://doi.org/10.1098/rspa.1953.0064>
- Gaina, C., Roest, W. R., & Müller, R. D. (2002). Late Cretaceous–Cenozoic deformation of northeast Asia. *Earth and Planetary Science Letters*, 197(3), 273–286. [https://doi.org/10.1016/S0012-821X\(02\)00499-5](https://doi.org/10.1016/S0012-821X(02)00499-5)
- Gale, A. S., Mutterlose, J., Batenburg, S., Gradstein, F. M., Agterberg, F. P., Ogg, J. G., & Petrizzo, M. R. (2020). The Cretaceous period. In F. M. Gradstein, J. G. Ogg, M. D. Schmitz, & G. M. Ogg (Eds.), *Geologic time scale 2020* (pp. 1023–1086).
- Gallet, Y., & Pavlov, V. E. (2016). Three distinct reversing modes in the geodynamo. *Izvestiya, Physics of the Solid Earth*, 52(2), 291–296. <https://doi.org/10.1134/S106935131602004X>
- Gallet, Y., Pavlov, V. E., & Korovnikov, I. (2019). Extreme geomagnetic reversal frequency during the Middle Cambrian as revealed by the magnetostratigraphy of the Khorbusuonka section (northeastern Siberia). *Earth and Planetary Science Letters*, 528, 115823. <https://doi.org/10.1016/j.epsl.2019.115823>
- Gao, W., Ciobanu, C. L., Cook, N. J., Slattery, A., Huang, F., & Song, D. (2019). Nanoscale study of titanomagnetite from the Panzihua Layered intrusion, Southwest China: Multistage Exsolution record ore formation. *Minerals*, 9(9), 1–26. <https://doi.org/10.3390/min9090513>
- Granot, R., Dymant, J., & Gallet, Y. (2012). Geomagnetic field variability during the Cretaceous normal superchron. *Nature Geoscience*, 5(3), 220–223. <https://doi.org/10.1038/ngeo1404>
- Granot, R., Tauxe, L., Gee, J. S., & Ron, H. (2007). A view into the Cretaceous geomagnetic field from analysis of gabbros and submarine glasses. *Earth and Planetary Science Letters*, 256(1–2), 1–11. <https://doi.org/10.1016/j.epsl.2006.12.028>
- Handford, B. T., Biggin, A. J., Haldan, M. M., & Langereis, C. G. (2021). Analyzing Triassic and permian geomagnetic paleosecular variation and the implications for ancient field Morphology. *Geochemistry, Geophysics, Geosystems*, 22(11), e2021GC009930. <https://doi.org/10.1029/2021gc009930>
- He, H., Deng, C., Wang, P., Pan, Y., & Zhu, R. (2012). Toward age determination of the termination of the Cretaceous Normal Superchron. *Geochemistry, Geophysics, Geosystems*, 13(2), Q02002. <https://doi.org/10.1029/2011GC003901>
- Henderson, C. M., Shen, S. Z., Gradstein, F. M., & Agterberg, F. P. (2020). The permian period. In F. M. Gradstein, J. G. Ogg, M. D. Schmitz, & G. M. Ogg (Eds.), *Geologic time scale 2020* (pp. 875–902).
- Hesselbo, S. P., Ogg, J. G., Ruhl, M., Hinnov, L. A., & Huang, C. J. (2020). The Jurassic period. In F. M. Gradstein, J. G. Ogg, M. D. Schmitz, & G. M. Ogg (Eds.), *Geologic time scale 2020* (pp. 955–1021).
- Hulot, G., & Gallet, Y. (1996). On the interpretation of virtual geomagnetic pole (VGP) scatter curves. *Physics of the Earth and Planetary Interiors*, 95(1–2), 37–53. [https://doi.org/10.1016/0031-9201\(95\)03106-5](https://doi.org/10.1016/0031-9201(95)03106-5)
- Ingham, E., Heslop, D., Roberts, A. P., Hawkins, R., & Sambridge, M. (2014). Is there a link between geomagnetic reversal frequency and paleointensity? A Bayesian approach. *Journal of Geophysical Research: Solid Earth*, 119(7), 5290–5304. <https://doi.org/10.1002/2014JB010947>

- Kirschvink, J. L. (1980). The least-squares line and plane and the analysis of palaeomagnetic data. *Geophysical Journal of the Royal Astronomical Society*, 62(3), 699–718. <https://doi.org/10.1111/j.1365-246X.1980.tb02601.x>
- Konstantinov, K. M., Bazhenov, M. L., Fetisova, A. M., & Khutorsky, M. D. (2014). Paleomagnetism of trap intrusions, East Siberia: Implications to flood basalt emplacement and the Permo–Triassic crisis of biosphere. *Earth and Planetary Science Letters*, 394, 242–253. <https://doi.org/10.1016/j.epsl.2014.03.029>
- Kulakov, E. V., Sprain, C. J., Doubrovine, P. V., Smirnov, A. V., Paterson, G. A., Hawkins, L., et al. (2019). Analysis of an updated paleointensity database (Q_{PI} -PINT) for 65–200 Ma: Implications for the long-term history of dipole moment through the Mesozoic. *Journal of Geophysical Research: Solid Earth*, 124(10), 9999–10022. <https://doi.org/10.1029/2018JB017287>
- Latyshev, A. V., Veselovskiy, R. V., & Ivanov, A. V. (2018). Paleomagnetism of the Permian-Triassic intrusions from the Tunguska syncline and the Angara-Taseeva depression, Siberian Traps large igneous province: Evidence of contrasting styles of magmatism. *Tectonophysics*, 723, 41–55. <https://doi.org/10.1016/j.tecto.2017.11.035>
- Lawrence, K. P., Tauxe, L., Staudigel, H., Constable, C. G., Koppers, A., McIntosh, W., & Johnson, C. L. (2009). Paleomagnetic field properties at high southern latitude. *Geochemistry, Geophysics, Geosystems*, 10(1), Q01005. <https://doi.org/10.1029/2008GC002072>
- Lebedev, I. E., Bobrovnikova, E. M., Tikhomirov, P. L., Eid, B., Lhuillier, F., & Pavlov, V. E. (2022). Amplitude of secular geomagnetic variation in late Cretaceous based on paleomagnetic studies of the Okhotsk–Chukotka volcanic belt from upper reaches of Malyi Anyui river, West Chukotka. *Izvestiya, Physics of the Solid Earth*, 58(2), 185–202. <https://doi.org/10.1134/S1069351322020045>
- Lebedev, I. E., Tikhomirov, P. L., Pasenko, A. M., Eid, B., Lhuillier, F., & Pavlov, V. E. (2021). New paleomagnetic data on late Cretaceous Chukotka volcanics: The Chukotka block probably underwent displacements relative to the North American and Eurasian plates after the formation of the Okhotsk-Chukotka volcanic belt? *Izvestiya, Physics of the Solid Earth*, 57(2), 232–246. <https://doi.org/10.1134/S1069351321020014>
- Lhuillier, F., & Gilder, S. A. (2013). Quantifying paleosecular variation: Insights from numerical dynamo simulations. *Earth and Planetary Science Letters*, 382, 87–97. <https://doi.org/10.1016/j.epsl.2013.08.048>
- Lhuillier, F., & Gilder, S. A. (2019). Palaeomagnetism and geochronology of Oligocene and Miocene volcanic sections from Ethiopia: Geomagnetic variability in the Afro-Arabian region over the past 30 Ma. *Geophysical Journal International*, 216(2), 1446–1481. <https://doi.org/10.1093/gji/ggy517>
- Lhuillier, F., Gilder, S. A., Wack, M., He, K., Petersen, N., Singer, B. S., et al. (2016). More stable yet bimodal geodynamo during the Cretaceous superchron? *Geophysical Research Letters*, 43(12), 6170–6177. <https://doi.org/10.1002/2016GL069303>
- Lhuillier, F., Lebedev, I. E., Tikhomirov, P. L., & Pavlov, V. E. (2023). High-latitude geomagnetic secular variation at the end of the Cretaceous normal superchron recorded by volcanic flows from the Okhotsk-Chukotka volcanic belt [Dataset]. Magnetics Information Consortium (MagIC). <https://doi.org/10.7288/V4/MAGIC/19774>
- Lhuillier, F., Shcherbakov, V. P., & Sycheva, N. K. (2023). Detecting dipolarity of the geomagnetic field in the paleomagnetic record. *Proceedings of the National Academy of Sciences of the United States of America*, 120(25), e2220887120. <https://doi.org/10.1073/pnas.2220887120>
- Lowrie, W., & Kent, D. V. (2004). Geomagnetic polarity timescales and reversal frequency regimes. In J. E. T. Channell, D. V. Kent, W. Lowrie, & J. G. Meert (Eds.), *Timescales of the paleomagnetic field* (pp. 117–129). AGU.
- McFadden, P. L., Merrill, R. T., & McElhinny, M. W. (1988). Dipole/quadrupole family modeling of paleosecular variation. *Journal of Geophysical Research*, 93(B10), 11583–11588. <https://doi.org/10.1029/JB093iB10p11583>
- McFadden, P. L., Merrill, R. T., McElhinny, M. W., & Lee, S. (1991). Reversals of the Earth's magnetic field and temporal variations of the dynamo families. *Journal of Geophysical Research*, 96(B3), 3923–3933. <https://doi.org/10.1029/90JB02275>
- Metelkin, D. V., Kazansky, A. Y., Bragin, V. Y., Tsel'movich, V. A., Lavrenchuk, A. V., & Kungurtsev, L. V. (2007). Paleomagnetism of the late Cretaceous intrusions from the Minusa trough (southern Siberia). *Russian Geology and Geophysics*, 48(2), 185–198. <https://doi.org/10.1016/j.rgg.2006.03.001>
- Nokleberg, W. J., Parfenov, L. M., Monger, J. W. H., Norton, I. O., Khanchuk, A. I., Stone, D. B., et al. (2000). Phanerozoic tectonic evolution of the circum-North Pacific (1044–9612). Retrieved from <https://pubs.usgs.gov/pp/2000/1626/>
- Ogg, J. G. (2020). Geomagnetic polarity time scale. In F. M. Gradstein, J. G. Ogg, M. D. Schmitz, & G. M. Ogg (Eds.), *Geologic time scale 2020* (pp. 159–192).
- Ogg, J. G., Chen, Z. Q., Orchard, M. J., & Jiang, H. S. (2020). The Triassic period. In F. M. Gradstein, J. G. Ogg, M. D. Schmitz, & G. M. Ogg (Eds.), *Geologic time scale 2020* (pp. 903–953).
- Otofuji, Y.-I., Zaman, H., Shogaki, G., Seki, H., Polin, V. F., Miura, D., et al. (2015). Paleomagnetism of the late Cretaceous ignimbrite from the Okhotsk-Chukotka volcanic belt, Kolyma-Omolon composite terrane: Tectonic implications. *Journal of Geodynamics*, 91, 1–12. <https://doi.org/10.1016/j.jog.2015.03.003>
- Özdemir, Ö. (1987). Inversion of titanomaghemites. *Physics of the Earth and Planetary Interiors*, 46(1), 184–196. [https://doi.org/10.1016/0031-9201\(87\)90181-6](https://doi.org/10.1016/0031-9201(87)90181-6)
- Pavlov, V. E., & Gallet, Y. (2005). A third superchron during the Early Paleozoic. *Episodes*, 28(2), 78–84. <https://doi.org/10.18814/epiugs/2005/v28i2/001>
- Petersen, N., & Vali, H. (1987). Observation of shrinkage cracks in ocean floor titanomagnetites. *Physics of the Earth and Planetary Interiors*, 46(1–3), 197–205. [https://doi.org/10.1016/0031-9201\(87\)90182-8](https://doi.org/10.1016/0031-9201(87)90182-8)
- Pick, T., & Tauxe, L. (1993). Geomagnetic palaeointensities during the Cretaceous normal superchron measured using submarine basaltic glass. *Nature*, 366(6452), 238–242. <https://doi.org/10.1038/366238a0>
- Prévot, M., Derder, M. E.-M., McWilliams, M., & Thompson, J. (1990). Intensity of the Earth's magnetic field: Evidence for a Mesozoic dipole low. *Earth and Planetary Science Letters*, 97(1–2), 129–139. [https://doi.org/10.1016/0012-821X\(90\)90104-6](https://doi.org/10.1016/0012-821X(90)90104-6)
- Sakhno, V. G., Polin, V. F., Akinin, V. V., Sergeev, S. A., Alenicheva, A. A., Tikhomirov, P. L., & Moll-Stalcup, E. J. (2010). The diachronous formation of the Enmyvaam and Amguema-Kanchalan volcanic fields in the Okhotsk-Chukotka volcanic belt (NE Russia): Evidence from isotopic data. *Doklady Earth Sciences*, 434(1), 1172–1178. <https://doi.org/10.1134/S1028334X10090072>
- Shcherbakova, V. V., Bakhmutov, V. G., Shcherbakov, V. P., Zhidkov, G. V., & Shpyra, V. V. (2012). Palaeointensity and palaeomagnetic study of Cretaceous and Palaeocene rocks from Western Antarctica. *Geophysical Journal International*, 189(1), 204–228. <https://doi.org/10.1111/j.1365-246X.2012.05357.x>
- Sokolov, S. D. (2010). Tectonics of northeast Asia: An overview. *Geotectonics*, 44(6), 493–509. <https://doi.org/10.1134/s001685211006004x>
- Sokolov, S. D., Tuchkova, M. I., Ganelin, A. V., Bondarenko, G. E., & Layer, P. (2015). Tectonics of the South Anyui suture, northeastern Asia. *Geotectonics*, 49(1), 3–26. <https://doi.org/10.1134/s0016852115010057>
- Stone, D. B., Layer, P. W., & Raikovich, M. I. (2009). Age and paleomagnetism of the Okhotsk-Chukotka volcanic belt (OCVB) near lake El'gygytyn, Chukotka, Russia. In *Stephan Mueller special publication series* (Vol. 4, pp. 243–260). <https://doi.org/10.5194/smsps-4-243-2009>
- Tarduno, J. A. (1990). Brief reversed polarity interval during the Cretaceous normal polarity superchron. *Geology*, 18(8), 683–686. [https://doi.org/10.1130/0091-7613\(1990\)018<0683:BRPIDT>2.3.CO;2](https://doi.org/10.1130/0091-7613(1990)018<0683:BRPIDT>2.3.CO;2)

- Tarduno, J. A., & Cottrell, R. D. (2005). Dipole strength and variation of the time-averaged reversing and nonreversing geodynamo based on Thellier analyses of single plagioclase crystals. *Journal of Geophysical Research*, *110*, B11. <https://doi.org/10.1029/2005jb003970>
- Tarduno, J. A., Cottrell, R. D., & Smirnov, A. V. (2001). High geomagnetic intensity during the Mid-Cretaceous from Thellier analyses of single plagioclase crystals. *Science*, *291*(5509), 1779–1783. <https://doi.org/10.1126/science.1057519>
- Tarduno, J. A., Cottrell, R. D., & Smirnov, A. V. (2002). The Cretaceous superchron geodynamo: Observations near the tangent cylinder. *Proceedings of the National Academy of Sciences of the United States of America*, *99*(22), 14020–14025. <https://doi.org/10.1073/pnas.222373499>
- Tarduno, J. A., Lowrie, W., Sliter, W. V., Bralower, T. J., & Heller, F. (1992). Reversed polarity characteristic magnetizations in the Albanian Contessa section, umbrian Apennines, Italy: Implications for the existence of a Mid-Cretaceous mixed polarity interval. *Journal of Geophysical Research*, *97*(B1), 241–271. <https://doi.org/10.1029/91JB02257>
- Tauxe, L., & Kent, D. V. (2004). A simplified statistical model for the geomagnetic field and the detection of shallow bias in paleomagnetic inclinations: Was the ancient magnetic field dipolar? In *Timescales of the paleomagnetic field* (pp. 101–115). AGU.
- Tauxe, L., & Staudigel, H. (2004). Strength of the geomagnetic field in the Cretaceous normal superchron: New data from submarine basaltic glass of the Troodos Ophiolite. *Geochemistry, Geophysics, Geosystems*, *5*(2), Q02H06. <https://doi.org/10.1029/2003GC000635>
- Tauxe, L., & Watson, G. S. (1994). The fold test: An eigen analysis approach. *Earth and Planetary Science Letters*, *122*(3–4), 331–341. [https://doi.org/10.1016/0012-821X\(94\)90006-X](https://doi.org/10.1016/0012-821X(94)90006-X)
- Thomson, B., Téllez C, C., Dietrich, A., Oliver, N. H. S., Akinin, V., Blenkinsop, T. G., et al. (2021). The Dvoinoye and September Northeast high-grade epithermal Au–Ag veins, Vodorzdelnaya district, Chukotka region, Russia. *Mineralium Deposita*, *57*(3), 353–376. <https://doi.org/10.1007/s00126-021-01065-0>
- Tikhomirov, P. L. (2020a). Cretaceous boundary-continental magmatism of Asian North-East and Genesis problems of the biggest Phanerozoic provinces of siliceous volcanism, Moscow.
- Tikhomirov, P. L. (2020b). Меловой окраинно-континентальный магматизм Северо-Востока Азии и вопросы генезиса крупнейших фанерозойских провинций кремнекислого вулканизма (р. 376). GEOS.
- Tikhomirov, P. L., Kalinina, E. A., Moriguti, T., Makishima, A., Kobayashi, K., Cherepanova, I. Y., & Nakamura, E. (2012). The Cretaceous Okhotsk–Chukotka Volcanic Belt (NE Russia): Geology, geochronology, magma output rates, and implications on the genesis of silicic LIPs. *Journal of Volcanology and Geothermal Research*, *221*–222, 14–32. <https://doi.org/10.1016/j.jvolgeores.2011.12.011>
- Tikhomirov, P. L., Lebedev, I. E., Lhuillier, F., & Pavlov, V. (2021). Stratigraphy of the Okhotsk–Chukotka belt (headwaters of Malyy Anyui river, the vicinity of Kupol deposit): U–Pb and ⁴⁰Ar/³⁹Ar age data. *Doklady Earth Sciences*, *501*(2), 1059–1064. <https://doi.org/10.1134/S1028334X2112014X>
- Tikhomirov, P. L., Pravikova, N. V., & Bychkova, Y. V. (2020). The Chukotka segment of the Uda–Murgal and Okhotsk–Chukotka volcanic belts: Age and tectonic Environment. *Russian Geology and Geophysics*, *61*(4), 378–395. <https://doi.org/10.15372/rgg2019149>
- Tikhomirov, P. L., Prokof'ev, V. Y., Kal'ko, I. A., Apletalin, A. V., Nikolaev, Y. N., Kobayashi, K., & Nakamura, E. (2017). Post-collisional magmatism of western Chukotka and Early Cretaceous tectonic rearrangement in northeastern Asia. *Geotectonics*, *51*(2), 131–151. <https://doi.org/10.1134/S0016852117020054>
- Tivey, M. A., Sager, W. W., Lee, S.-M., & Tominaga, M. (2006). Origin of the Pacific Jurassic quiet zone. *Geology*, *34*(9), 789. <https://doi.org/10.1130/G22894.1>
- Tominaga, M., Sager, W. W., Tivey, M. A., & Lee, S.-M. (2008). Deep-tow magnetic anomaly study of the Pacific Jurassic Quiet Zone and implications for the geomagnetic polarity reversal timescale and geomagnetic field behavior. *Journal of Geophysical Research*, *113*(B7), B07110. <https://doi.org/10.1029/2007jb005527>
- Torsvik, T. H., Van der Voo, R., Preeden, U., Mac Niocaill, C., Steinberger, B., Doubrovine, P. V., et al. (2012). Phanerozoic polar wander, palaeogeography and dynamics. *Earth-Science Reviews*, *114*(3–4), 325–368. <https://doi.org/10.1016/j.earscirev.2012.06.007>
- Tuchkova, M. I., Shokalsky, S. P., Petrov, O. V., Sokolov, S. D., Sergeev, S. A., & Moiseev, A. V. (2020). Triassic deposits of Chukotka, Wrangel island and Mendeleev rise, Arctic Sea: Sedimentology and geodynamic implications. *GFF*, *142*(2), 158–168. <https://doi.org/10.1080/11035897.2020.1724668>
- Vandamme, D. (1994). A new method to determine paleosecular variation. *Physics of the Earth and Planetary Interiors*, *85*(1–2), 131–142. [https://doi.org/10.1016/0031-9201\(94\)90012-4](https://doi.org/10.1016/0031-9201(94)90012-4)
- Veselovskiy, R. V., Dubinya, N. V., Ponomarev, A. V., Fokin, I. V., Patonin, A. V., Pasenko, A. M., et al. (2022). Shared Research facilities "Petrophysics, Geomechanics and paleomagnetism" of the Schmidt Institute of Physics of the Earth ras. *Geodynamics & Tectonophysics*, *13*(2). <https://doi.org/10.5800/gt-2022-13-2-0579>
- Wang, T., Ramezani, J., Wang, C., Wu, H., He, H., & Bowring, S. A. (2016). High-precision U–Pb geochronologic constraints on the Late Cretaceous terrestrial cyclostratigraphy and geomagnetic polarity from the Songliao Basin, Northeast China. *Earth and Planetary Science Letters*, *446*, 37–44. <https://doi.org/10.1016/j.epsl.2016.04.007>
- Watson, G. S. (1983). Large sample theory of the Langevin distribution. *Journal of Statistical Planning and Inference*, *8*(3), 245–256. [https://doi.org/10.1016/0378-3758\(83\)90043-5](https://doi.org/10.1016/0378-3758(83)90043-5)
- Wu, H., Zhang, S., Jiang, G., Hinnov, L., Yang, T., Li, H., et al. (2013). Astrochronology of the early Turonian–early Campanian terrestrial succession in the Songliao basin, northeastern China and its implication for long-period behavior of the solar System. *Palaeogeography, Palaeoclimatology, Palaeoecology*, *385*, 55–70. <https://doi.org/10.1016/j.palaeo.2012.09.004>
- Zijderveld, J. D. A. (1967). A.C. Demagnetization of rocks: Analysis of results. In D. Collinson, K. M. Creer, & S. K. Runcorn (Eds.), *Methods in paleomagnetism* (pp. 254–286). Elsevier.